



Contribution of free tropospheric aerosols to Arctic low-level cloud droplets formation and longwave radiative forcing

Roman Pohorsky¹, Heather Guy^{2,3}, Ian Morley Brooks², Lea Haberstock^{4,5}, Nicolas Fauré⁶, Paul Zieger^{4,5}, Julia Kojó^{4,5}, Sonja Murto^{5,7,8}, Radiance Calmer¹, Benjamin Heutte¹, Michael Lonardi¹, Erik Schurch Thomson⁶, Michael Tjernström^{5,7}, Jessie Creamean⁹, Athanasios Nenes¹⁰, Julia Schmale¹

¹Extreme Environments Research Laboratory, Ecole Polytechnique Fédérale de Lausanne, Sion, 1950, Switzerland

²School of Earth and Environment, University of Leeds, Leeds, LS2 9JT, U.K.

³National Centre for Atmospheric Science, Leeds, LS2 9JT, U.K.

⁴Department of Environmental Science, Stockholm University, Stockholm, SE-106 91, Sweden

⁵Bolin Centre for Climate Research, Stockholm University, Stockholm, SE-106 91, Sweden

⁶Department of Chemistry and Molecular Biology, University of Gothenburg, Gothenburg, SE-41390, Sweden

⁷Department of Meteorology, Stockholm University, Stockholm, SE-106 91, Sweden

⁸Department of Earth Sciences, Uppsala University, Uppsala, SE-75236, Sweden

⁹Department of Atmospheric Science, Colorado State University, Fort Collins, CO, 80523, USA

¹⁰Laboratory of Atmospheric Processes and their Impacts, Ecole Polytechnique Fédérale de Lausanne, Lausanne, 1015, Switzerland

Correspondence to: Roman Pohorsky (roman.pohorsky@epfl.ch) and Julia Schmale (julia.schmale@epfl.ch)

Abstract. Aerosol-cloud-radiation interactions are a major source of uncertainty in the Arctic climate, particularly for low-level clouds (LLC) that dominate cloud cover. This study presents in situ measurements of aerosols and cloud droplets collected with a tethered-balloon between May 16 and June 10, 2023, during the Atmospheric Rivers and the onset of sea ice MELT campaign above sea ice in the Fram Strait. The objective was to quantify the contributions of boundary-layer and free-tropospheric sources to the cloud condensation nuclei (CCN) budget of LLCs. Above- and below-cloud observations of five LLCs showed enhanced aerosol concentrations above cloud top in four cases.

The analysis of a case study, in which the cloud was coupled to the surface, revealed a complex layered structure of aerosol properties, including multiple distinct size distributions. Aerosol concentrations above the cloud were up to four times higher than below, and measurements at the cloud-top interface indicated mixing between in-cloud and free-tropospheric air masses. Simulations of cloud droplet concentrations based on measured particle size distributions showed that including aerosols from above cloud, rather than only below, was required to achieve closure with observations. Our highly detailed observations around the cloud allowed us to demonstrate the significance of free-tropospheric CCN sources, which influence Arctic cloud microphysical and radiative properties. Concretely, not accounting for free tropospheric CCN would have resulted in a low bias in the longwave radiative forcing of 1.3 W m^{-2} . These findings highlight the need for systematic vertical aerosol observations and improved model representation of elevated aerosol layers.



34 **1 Introduction**

35 The Arctic climate is changing rapidly, and the surface energy budget (SEB) is highly dependent on the presence of clouds
36 and their macro and microphysical properties (e.g., Intrieri et al., 2002; Sedlar et al., 2011; Tjernström et al., 2008). In the
37 Arctic, low-level mixed-phase and liquid stratocumulus clouds (referred to hereafter as low-level clouds (LLCs) for simplicity)
38 commonly occur year-round (Mioche et al., 2015; Morrison et al., 2012; Shupe, 2011). Clouds affect both the downwelling
39 shortwave radiative fluxes by reflecting incoming solar radiation and net longwave radiation by radiating towards the surface
40 as black bodies. While clouds generally have a cooling effect globally, Arctic LLCs above snow-covered sea ice lead to positive
41 radiative forcing for much of the year (Shupe and Intrieri, 2004). This is because positive longwave radiative forcing dominates
42 over negative shortwave forcing due to absence of sunlight in winter (Curry et al., 1993; Intrieri et al., 2002; Kay et al., 2016;
43 Sedlar et al., 2011), and high surface albedo in summer and low solar zenith angle (except for a short period when the sea ice
44 includes many melt ponds). Although the importance of clouds for the Arctic SEB is well established, accurately simulating
45 their radiative forcing remains difficult with models (Young McCusker et al., 2023). As a result, cloud-related radiative fluxes
46 constitute the largest source of errors in Arctic SEB predictions (Sedlar et al., 2020; Solomon et al., 2023; Tjernström et al.,
47 2008).

48 One of the sources of this uncertainty arises from aerosol-cloud interactions, whose representation in models remains
49 challenging (Morrison et al., 2012; Tjernström et al., 2008). Aerosols play crucial roles in modulating cloud properties by
50 acting as cloud condensation nuclei (CCN) that form liquid droplets and ice-nucleating particles (INPs) that form ice crystals.
51 Their presence can influence cloud formation, total condensate amount, phase partitioning, lifetime, dynamics and radiative
52 effects (e.g., Fan et al., 2016; Lohmann and Feichter, 2005). Accurate knowledge of the aerosol properties that seed clouds is
53 therefore fundamental.

54 In the Arctic, above sea ice, aerosol concentrations can be low, limiting the formation of clouds (e.g., Bigg et al., 1996; Boyer
55 et al., 2023; Creamean et al., 2022; Lannefors et al., 1983; Mauritsen et al., 2011). Furthermore, frequent surface-based or low-
56 level temperature inversions (Akansu et al., 2023; Bradley et al., 1992; Jozef et al., 2024) and decoupling layers (i.e., vertically
57 discontinuous turbulent mixing) between the surface and LLCs can inhibit the supply of aerosols from local surface sources
58 upwards to the clouds (Brooks et al., 2017; Shupe et al., 2013). Under these conditions, ground-based measurements of aerosols
59 are not necessarily representative of the aerosols seeding the clouds (Creamean et al., 2021). Given the specific conditions of
60 the Arctic, the free troposphere can constitute an alternative important source of CCN and INPs for cloud formation and
61 sustainment (Igel et al., 2017), much like humidity inversions above clouds have been shown to sustain Arctic LLCs (Solomon
62 et al., 2014).

63 The importance of elevated aerosol layers located above cloud top has already been observed in previous studies like
64 Kupiszewski et al. (2013) and Pilz et al. (2024) who performed vertical measurements of size-resolved aerosol concentrations
65 in the Arctic. They measured increasing aerosol concentrations with altitude in the free troposphere on several occasions. The
66 observed concentrations for CCN-sized particles were up to an order of magnitude greater than within the boundary layer.



67 Their studies showed higher aerosol concentrations in the free troposphere than within the boundary layer on several occasions.
68 These layers had concentrations of up to about an order of magnitude greater than within the boundary layer for CCN-sized
69 particles. In a modeling study, Price et al. (2023) found that aerosols from remote sources, entrained into the boundary layer
70 from the free troposphere, accounted for nucleation (< 10 nm) and Aitken (10 – 100 nm) mode particle concentrations that
71 were otherwise underestimated by the model. In another study, using large-eddy simulations, Igel et al. (2017) showed that
72 when layers of enhanced aerosol number concentrations were present above Arctic LLCs, these particles could activate at
73 cloud top and be entrained into the cloud. Thereby they showed that aerosol properties at the surface were not always a good
74 indicator of all aerosol particles feeding the cloud.

75 Despite mounting evidence that more concentrated aerosol layers above Arctic LLCs are common and that entrainment from
76 the free troposphere can replenish boundary-layer aerosol, key uncertainties remain regarding how frequently this pathway is
77 relevant across the Arctic and how strongly it perturbs cloud microphysical and radiative properties. Observational evidence
78 for enhanced aerosol concentrations aloft has often relied on limited observations and did not provide a direct microphysical
79 closure linking CCN availability above cloud to in-cloud droplet number concentrations or resulting radiative properties
80 (Creamean et al., 2021; Kupiszewski et al., 2013; Pilz et al., 2024). Hence, an important outstanding question is whether and
81 when entrainment of free-tropospheric aerosol in LLCs measurably alters cloud droplet activation and the associated radiative
82 properties of the LLCs.

83 To answer these questions, we first need more extensive profiling observations of CCN, INP and cloud microphysical
84 properties (Kretzschmar et al., 2020; Sedlar et al., 2020; Wendisch et al., 2023) in order to characterize the aerosol seeding of
85 clouds, their origin and under which conditions the aerosols at the surface are or are not representative of the aerosols in the
86 cloud layer and when aerosols in the free troposphere become important to consider.

87 In this study, we explicitly address the role of the free troposphere as a source of CCN (and by extension INPs, although not
88 explicitly analyzed here) for Arctic LLCs and investigate how accounting for this source modifies cloud microphysical and
89 longwave radiative properties compared to a framework that only considers boundary-layer aerosols. In particular, we aim to

90 (i) assess whether the free troposphere can supply a measurable addition of CCN for Arctic LLC formation and
91 sustainment, and

92 (ii) examine how cloud microphysical and radiative characteristics differ depending on whether aerosol sources above
93 the cloud are included.

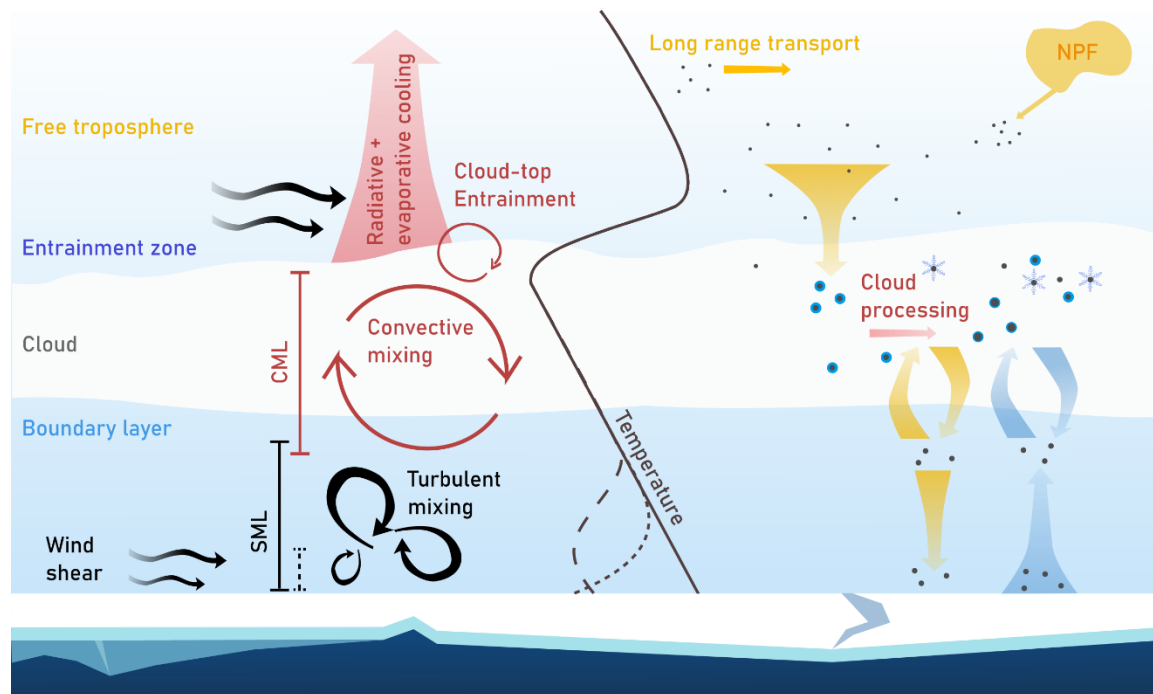
94 To address these questions, we follow a framework that links aerosol pathways to the thermodynamic and turbulent structure
95 of the cloud-topped Arctic boundary layer. The framework, illustrated in Fig. 1, includes the different Arctic LLC
96 components. In the lowest portion of the boundary layer a surface mixing layer (SML) is maintained just above the surface,
97 driven primarily by surface wind shear. At the upper part of the boundary layer and including LLCs themselves is a cloud
98 mixed layer (CML), where turbulence is driven by buoyant overturning within the clouds resulting from cloud top radiative
99 cooling. Turbulence at cloud top promotes entrainment of free tropospheric air. Depending on the extent of the layers,
100 turbulence may span the full boundary layer depth or be vertically discontinuous. The dynamics discussed here are critical to



101 understanding the influence of below- and above-cloud aerosol on the cloud properties as they determine from where aerosols
102 are mostly transported into the cloud. On the right, two aerosol pathways are shown. The first (represented by blue arrows)
103 only considers surface and boundary layer aerosols as an important source of CCN and INPs for the cloud and a re-circulation
104 of those particles between the cloud and the atmospheric column below. The second pathway (yellow arrows) also considers
105 the incorporation of free tropospheric aerosols as an additional significant source of CCN and INPs.

106 To investigate how relevant the free tropospheric pathway can be for Arctic LLCs and address the research questions stated
107 above, a tethered balloon-based platform, the Modular Multiplatform Air Compatible Measurement System (MoMuCAMS,
108 Pohorsky et al. 2024) was deployed during the 2023 Atmospheric Rivers and the onset of sea ice MELT (ARTofMELT,
109 Zieger, Tjernström et al. in prep) expedition. Tethered balloons are an advantageous platform for high-resolution vertical
110 measurements. They can carry significant instrument payloads (compared to drones), can hover at fixed altitudes and operate
111 in clouds even under icing conditions (e.g., Creamean et al., 2021; Pilz et al., 2022; Pohorsky et al., 2024). The deployment of
112 such balloons enables very detailed measurements between the surface and the lower free troposphere (altitudes that are often
113 too low for crewed aircraft). The ability of MoMuCAMS to measure the size distribution of nucleation, Aitken and
114 accumulation mode (100 – 1000 nm) particles (a novelty for tethered-balloon observations) is a distinction that is critical to
115 identifying different aerosol populations, observing aerosol processing in the vicinity of the clouds and better quantifying CCN
116 concentrations. Additionally, cloud droplet number concentration measurements are a direct characterization of clouds'
117 microphysical properties. Here, we leveraged the measurement and flying capabilities of the MoMuCAMS platform to perform
118 a closure analysis of cloud droplets, which was used to evaluate the role of CCN contributions from above an observed cloud.
119 That analysis is complemented with cloud droplet activation simulations and radiative transfer modeling to quantify how
120 different the microphysical and longwave radiative properties of the cloud are when considering cloud seeding from aerosol
121 particles located above.

122



123

124 **Figure 1** Schematic of low-level cloud over the pack ice in the Arctic. On the left, the different elements of the cloud-topped Arctic
125 boundary layer are illustrated, based on Fig. 2 from Brooks et al. (2017), including the surface mixing layer (SML), the convective
126 mixing layer (CML) and entrainment from cloud-top cooling. An idealized temperature profile represents a well-mixed boundary
127 layer for a cloud base coupled to the surface (full line) and two alternative situations with an elevated inversion below the cloud base
128 (long, dashed line) and a surface-based inversion (short, dashed lines). On the right, two idealized pathways of cloud-feeding aerosols
129 are depicted. Blue arrows represent a situation with only boundary layer contributions of cloud condensation nuclei (CCN) and ice-
130 nucleating particles (INP). Yellow arrows also include a contribution of free tropospheric aerosols from long-range transport or new
131 particle formation (NPF) to the cloud's CCN and INP budget.

132 2Methods

133 The ARTofMELT expedition took place in the Fram Strait onboard the Swedish icebreaker *Oden* from May 9 to June 13,
134 2023. The cruise began and ended in Longyearbyen and included two ice camps, where vertical measurements were performed
135 with a 45-m³ Helikite lifting the MoMuCAMS (Fig. 2). In total, 23 flights on 13 different days were carried out between May
136 16 and June 10 (see Table S1).

137 2.1 Helikite instrumentation

138 The in situ measurements were performed with the MoMuCAMS described in Pohorsky et al. (2024). It was deployed from a
139 container platform located on the aft deck of the ship (see Fig. 2c) and equipped with instruments to characterize aerosol and
140 cloud droplet properties. The maximum altitude reached was 645 m above sea level.

141 A miniaturized scanning electrical mobility spectrometer (mSEMS model 9404, Brechtel Manufacturing Inc., USA) provided
142 particle number size distribution (PNSD) measurements for particles with electrical mobility diameters between 8 and 280 nm



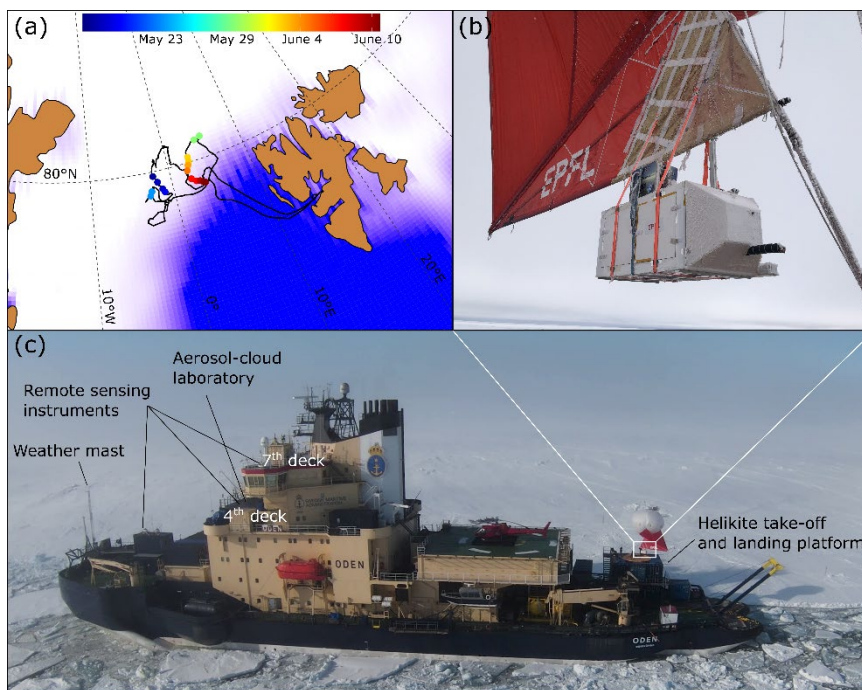
143 with 40 log-spaced size bins and a bin time of 4 seconds, yielding a time resolution of 2 min 40 sec per scan. A portable optical
144 particle spectrometer (POPS, Handix Scientific, USA) provided PNSD measurements for optical diameters between 186 and
145 3370 nm. The POPS was operated with 16 log-spaced size bins and a 1 Hz acquisition frequency.

146 A light optical aerosols counter (LOAC, Meteomodem, France) was installed on top of MoMuCAMS to measure the size
147 distribution of aerosols and cloud droplets from 200 nm up to 50 μm with a time resolution of 30 sec (Renard et al., 2016). In
148 the LOAC, two detectors measure the scattering, at 12° and 60°, produced by the sampled particles traveling through a laser
149 beam. The intensity of the forward scattering signal is used to measure the size of the particles and the difference between the
150 two angles provides additional information to classify particle types (e.g., carbonaceous, minerals, liquid droplets).

151 In addition to aerosol measurements, meteorological variables were measured during the flights. A wind probe (SmartTether,
152 Anasphere, USA) attached directly to the tether, \approx 1.5 meters below the MoMuCAMS collected wind speed and direction data
153 at 0.5 Hz. Two sensors (SHT85, Sensirion, CH), installed in an insulated and actively ventilated radiation shield casing attached
154 to the side of MoMuCAMS, measured temperature and relative humidity (RH). Pressure was recorded in triplicate by sensors
155 located on the MoMuCAMS's board computer (MPL115A2, Adafruit, USA), the SmartTether and the POPS. A summary of
156 deployed instruments for each flight during the campaign is listed in Table S1.

157 In addition, a single channel tricolor absorption photometer (STAP model 9406, Brechtel Manufacturing Inc., USA) measured
158 aerosol light absorption coefficients at 450, 525 and 624 nm, an 8-channel filter sampler (FILT model 9401, Brechtel
159 Manufacturing Inc., USA) collected aerosol particles on transmission electron microscopy copper grids and a filter sampler
160 (IcePuck, Handix, USA) collected aerosol particles on polycarbonate filters for INP analyses. The filter-sampling instruments
161 were deployed on some flights, but their data are not presented here.

162



163

164 **Figure 2 (a) Ship track and location of Helikite flights during the ARTofMELT campaign. The colored dots represents the Helikite**
165 **flights dates and locations. The white to blue ocean surface shading depicts the May 16, 2023 sea ice concentration (day of the first**
166 **Helikite flight). Data source: <https://www.ncei.noaa.gov/products/climate-data-records/sea-ice-concentration>. (b) Close-up view of**
167 **MoMuCAMS attached to the Helikite. The LOAC is placed on top of the enclosure. Photo credit: Roman Pohorsky. (c) The *IB Oden***
168 **moored to an ice floe with different measurement platforms indicated. Photo credit: Christopher Groop.**

169 2.2 Helikite data processing

170 Data processing followed the procedure described in Schmale et al. (submitted) based on the EBAS guidelines ([https://ebas-](https://ebas-submit.nilu.no/)
171 [submit.nilu.no/](https://ebas-submit.nilu.no/)). Raw mSEMS data files were inverted using a software package provided by the manufacturer. At level 0,
172 one data file per flight that includes the data from the different instruments, was created. At level 1, the meteorological variables
173 were cleaned for invalid data. Because the ship was warmed by incoming solar radiation, an influence on the temperature
174 profiles was observed in the first tens of meters. This influence was identified by a steeper temperature gradient relative to that
175 observed higher up. The altitude of influence on the temperature measurements was manually identified for each profile and
176 data below this altitude were flagged. Additionally, a corrected temperature profile was produced. The temperature profile was
177 reconstructed between the take-off altitude and the highest point of temperature influence by extrapolating the temperature
178 data above and assuming the same temperature gradient as the observed mean gradient. An example of the temperature
179 influence of the ship, data flagging and reconstructed temperature profile is shown in Fig. S1.

180 The altitude above sea level was calculated using the barometric formula,

181

$$182 \quad h_b = \frac{T_0}{L_0} \left(1 - \frac{p_b}{p_0} \right)^{\frac{L_0 R}{g}}, \quad (1)$$



183 where T_0 is the temperature at the surface, $L_0 = 6.5 \text{ K km}^{-1}$ is the mean environmental lapse rate, p_0 and p_b are the pressure at
184 the surface and balloon height, respectively, $R = 287 \text{ J kg}^{-1} \text{ K}^{-1}$ is the gas constant for dry air and g is the Earth's gravitational
185 constant.

186 Aerosol data were manually inspected for outliers and anomalous data, which were flagged and removed. An intercomparison
187 of the MoMuCAMS with the ship-based aerosol instruments (see Sect. 2.3) indicated an undercounting of aerosol number
188 concentration by the POPS (about 30 %). A size-dependent correction for aerosol counting was applied based on a comparison
189 with a differential mobility particle sizer (DMPS) during a ground-based intercomparison. Aerosol concentrations were then
190 converted to standard temperature and pressure using the temperature measured in the sampling line. Results of the comparison
191 and corrected size distribution are shown in Fig. S2 and correction factors are listed in Table S2.

192 For the cloud droplet size distribution and concentration, we selected 'particles' larger than $3 \mu\text{m}$, that were classified as
193 droplets by the LOAC. Concentrations for different bin sizes are normalized by the respective bin width ($dN \text{ dlog}(D_p)^{-1}$). A
194 comparison of the LOAC data with a fog monitor (FM120, Droplet Measurement Technologies, USA) is shown in Fig. S3.

195 Pollution from the ship exhaust was identified visually for each profile. Ship exhaust plumes were identified by strong and
196 rapid increases in the aerosol number concentration (typically between 30 and 50 m altitude). Polluted data points were flagged
197 and removed from the analysis. An example of a profile with flagged ship pollution is shown in Fig. S1.

198 Finally, a 10-second arithmetic averaging was applied to the data (except for the mSEMS and LOAC data with initial coarser
199 resolutions). For the analysis of vertical profiles presented in this study, the data were spatially averaged into 10-m altitude
200 bins and plotted at the midpoint altitude.

201

202 **2.3 Supporting data from *IB Oden***

203 To complement the analysis of the MoMuCAMS vertical profiles, ship-based remote sensing and in situ observations were
204 used. At the front of the ship's superstructure, on the fourth deck, the mobile aerosol-cloud laboratory container from
205 Stockholm University was equipped with a suite of aerosol instruments (see location in Fig. 2c). A differential mobility particle
206 spectrometer (DMPS) sampled from a total inlet (i.e., sampling all aerosol sizes), providing aerosol number size distribution
207 measurements for particles with an electrical mobility between 15 and 840 nm at a time resolution of 12 minutes (as in Karlsson
208 et al. 2022). A cloud condensation nuclei counter (CCNC, Droplet Measurement Technologies, USA) (Lance et al., 2006;
209 Roberts and Nenes, 2005) operated in parallel to measure the CCN concentration. The CCNC operated at supersaturations of
210 0.1, 0.2, 0.3, 0.5 and 1.0 % with a duration of 15 minutes per supersaturation level.

211 A suite of remote sensing instrumentation made continuous measurements throughout the cruise. A 94 GHz W-band Doppler
212 Cloud Radar (RPG-FMCW-94-SP, Radiometer Physics GmbH, Germany) was installed on top of a container on the 4th deck,
213 this provided measurements of radar backscatter and Doppler velocities with a vertical resolution between 7.45 and 28.6 m
214 (depending on range) and time resolution of approximately 5.4 seconds. A laser ceilometer (CL31, Vaisala, Finland) installed
215 on the 7th deck, provided measurements of cloud base every 30 seconds with a range resolution of 10 m. Liquid water path



216 was estimated by a microwave radiometer (HATPRO, Radiometer Physics GmbH, Germany). Here cloud boundaries are
217 derived from the cloud radar and laser ceilometer. Profiles of liquid water content are derived via the Cloudnet algorithm
218 (Illingworth et al., 2007) using data from the radar, ceilometer, HATPRO, and radiosondes. A HALO Photonics Streamline
219 Doppler Lidar (HALO Photonics, UK), installed above a container on the 2nd deck, was used to measure the vertical velocities
220 at cloud base and in the lower part of the cloud.

221 Radiosondes (RS41, Vaisala, Finland) were launched every 6 hours during the campaign (nominally at 05:30, 11:30, 17:30
222 and 23:30 UTC). Data from the radiosondes were used to complete meteorological data from the Helikite flights, which were
223 more sporadic in time and limited in altitude. The data used from the radiosoundings included pressure, temperature, and
224 relative and specific humidity.

225 Measurements of near surface meteorology (temperature, pressure, relative humidity, wind speed and wind direction,
226 upwelling and downwelling longwave and shortwave radiation) were obtained from a weather station composed of a
227 meteorological mast and a radiometer stand installed on the sea ice and from the ship's weather station (at 25 m altitude).

228 Finally, synoptic conditions were inspected with ERA5 data (Soci et al., 2024), and backward trajectory analysis data from the
229 Lagrangian analysis tool (LAGRANTO; Sprenger and Wernli, 2015) were used to determine the origin and influences of air
230 masses arriving at the ship location during Helikite flights. For each backward trajectory simulation, an ensemble of ≈ 37 5-
231 day trajectories was calculated. The arrival point of each trajectory was located in a 100 km circle around the ship's location
232 at 50 hPa above sea level. Shapes and tracks of surface cyclones were calculated on ERA5 dataset based on the MOAAP
233 tracking algorithm (Prein et al., 2023); continuous areas in the SLP anomaly field below -8 hPa and persisting for more than
234 12 hours are identified as cyclones.

236 **2.4 Temperature inversion and cloud coupling analysis**

237 Temperature profiles from radiosoundings and Helikite flights were analyzed to identify the heights of temperature inversions.
238 Inversions were identified by layers with a positive vertical temperature gradient ($dT/dz^{-1} > 0$) for at least 25 meters (Jozef et
239 al., 2022; Kahl, 1990). The temperature inversion height was used to characterize thermodynamic coupling between observed
240 LLCs and the surface. Following Pilz et al. (2024), a cloud is considered to be decoupled (thermodynamically) if a surface-
241 based inversion was detected or if the base of an elevated inversion was located below the cloud base.

243 **2.5 Cloud boundaries determination**

244 An inherent challenge in analyzing tethered-balloon profiles that extend through clouds is to accurately determine cloud base
245 and cloud top boundaries. In this study, we estimated these boundaries using a combination of relative humidity ($RH \approx 100\%$),
246 in-flight video recordings and observed aerosol concentrations. Within clouds the MoMuCAMS' low sampling flow rate means



247 that primarily interstitial aerosol (i.e., non-activated particles) is sampled, because cloud droplets are too heavy to be drawn
248 into instruments. Consequently, observed aerosol concentrations decreased within cloud layers.

249
250 To validate cloud boundary estimates, and monitor changes over time, we compared them with ceilometer-derived cloud base
251 heights and radar reflectivity data. An example of the cloud boundary determination is shown in Fig. S4. It should be noted
252 that cloud boundaries, particularly cloud base, are inherently diffuse, and their exact definition is subject to interpretation,
253 introducing an inherent uncertainty of approximately ± 30 m.

254

255 2.6 Droplet activation parametrization

256 We use an aerosol activation parametrization developed by Nenes and Seinfeld (2003) and further improved by Fountoukis
257 and Nenes (2005), Barahona et al. (2010) and Morales Betancourt and Nenes (2014) to calculate the number of cloud droplets
258 (N_d) formed in observed clouds and compare those values with the in situ LOAC measurements. The parametrization requires
259 aerosol PNSD, hygroscopicity, updraft velocity and environmental conditions at cloud height (pressure and temperature) as
260 inputs.

261 In the parametrization, we used the approach introduced by Morales and Nenes (2010) to calculate the probability density
262 function (PDF)-averaged N_d and supersaturation (s_{max}) in the cloud (which is representative of the measured droplet number
263 concentration) by applying the parametrization using a single characteristic velocity, $w^* = 0.79\sigma_w$ (Conant et al., 2004;
264 Fountoukis et al., 2007; Georgakaki et al., 2021; Motos et al., 2023). The σ_w is the standard deviation of a gaussian fit of the
265 vertical velocity data at cloud base obtained from the Doppler Lidar. To be representative of the variability of the vertical
266 velocity, the PDF is generated from data over one hour. The pressure and temperature data at cloud base are obtained from
267 Helikite and radiosonde measurements. For parametrizations with data collected between profiles, the Helikite and radiosonde
268 pressure and temperature measurements are interpolated.

269 The aerosol number size distribution data measured directly below cloud base (i.e. 50 m layer below cloud base) and in the
270 entrainment zone were used as inputs for different simulation scenarios. The PNSDs were fitted with lognormal distributions
271 using a multipeak fitting package in IGOR Pro v9.02 and reconstructed to fit the required number of bins assumed by the
272 parametrization scheme.

273 The hygroscopicity parameter (κ) was calculated from ship-based measurements of aerosol PNSD and CCN concentrations
274 following the method of Petters and Kreidenweis (2007),

$$275 \kappa = \frac{4A^3}{27D_d^3(\ln S_c)^2}, \quad (2)$$

276



277 where S_c is the critical saturation ratio ($S_c = \frac{ss_c}{100} + 1$), with ss_c = critical supersaturation in %. The critical dry diameter (D_d)
278 at each supersaturation was calculated by integrating the aerosol size distribution from the larger particle sizes to the lowest
279 until the integrated concentration matched the CCN concentration.

280 The A is defined as follows:

$$281 \quad A = \frac{4\sigma_a M_w}{RT\rho_w} \quad (3)$$

282 where the surface tension of water in air $\sigma_a = 0.072 \frac{J}{m^2}$ and the temperature of $T = 298.15$ K is used. $\rho_w = 997 \frac{kg}{m^3}$ is the
283 density of water, $M_w = 18.015 * 10^{-3} \frac{kg}{mol}$ is the molecular weight of water and $R = 8.3145 \frac{J}{mol \cdot K}$ is the ideal gas constant.

284 2.7 Radiative transfer modeling

285 To assess clouds' influence on downwelling longwave radiation in response to the number and size of cloud droplets, radiative
286 transfer modeling (RTM) was performed. We used a plane-parallel radiative transfer model with the DISORT solver (Stamnes
287 et al., 1988) implemented in the libRadtran 2.0.6 software package (Emde et al., 2016; Mayer and Kylling, 2005). Simulations
288 were performed with the LOWTRAN parametrization for gaseous absorption (Ricchiazzi et al., 1998). For aerosols, we used
289 standard maritime profiles based on the model of (Shettle, 1990). The season was set to "summer". Temperature and relative
290 humidity profiles were based on radiosoundings and complemented with Helikite measurements in the lower layers as in
291 Lonardi et al. (2024).

292 A profile of liquid water content (LWC) and droplet effective radius (r_{eff}) is included to account for cloud effects on radiation.
293 The r_{eff} is obtained as in Lonardi et al. (2024),

$$294 \quad r_{eff} = \left[\frac{3}{4\pi \cdot \rho_w \cdot N_d \cdot k} \cdot LWC(z) \right]^{\frac{1}{3}}, \quad (4)$$

295 where ρ_w is the density of liquid water and the parameter k converts the effective droplet radius into the volumetric droplet
296 radius and was set to 0.8, which is representative for stratocumulus clouds (Brenguier et al., 2011). The LWC was retrieved
297 from remote sensing data and r_{eff} was calculated by assuming a constant N_d profile throughout the cloud column.

299 3 Overview of meteorological conditions, aerosols and clouds during ARTofMELT

300 We present here an overview of the conditions during the ARTofMELT campaign to provide a broader context for the
301 following analysis of a case study. A more complete overview of the entire campaign is provided in Zieger et al. (in prep).
302 Figure 3 shows near surface meteorology, cloud conditions, surface radiation and aerosol concentrations between May 16
303 (establishment of the first ice camp) and June 13 (ship leaving the ice).



304 During the first days, the temperature rose from $-14\text{ }^{\circ}\text{C}$ to just above $0\text{ }^{\circ}\text{C}$ on May 20 (Fig. 3a). It then varied between 0 and
305 $-8\text{ }^{\circ}\text{C}$ until June 10, when it again exceeded $0\text{ }^{\circ}\text{C}$, coinciding with the onset of sea-ice melt (Zieger et al., in prep). The relative
306 humidity was continuously high with values usually exceeding 80 %.

307 Overall, a cloud fraction above 5 oktas (representing a cloudy sky) represented 64 % of the observation period (Fig. 3c). Within
308 these cloudy conditions, a cloud base below 2000 m was detected 97 % of the time. Although some of these clouds might have
309 been deep frontal clouds, Fig. 3b shows that clouds with a base below 2000 m were mainly shallow stratiform clouds. The
310 cloudiness during ARTofMELT falls at the lower end of cloud fractions reported during major Arctic field campaigns such as
311 the Surface Heat Budget of the Arctic Ocean campaign (SHEBA, $\approx 88\text{ }%$ monthly average in May and June; Intrieri et al.
312 2002), the Arctic Ocean 2018 (AO2018, $\approx 96\text{ }%$ cloud occurrence in August and September; Vüllers et al. 2021), and the
313 Multidisciplinary drifting Observatory for the Study of Arctic Climate (MOSAiC, 74 and 82 % cloud occurrence in May and
314 June, respectively; Achtert et al. 2025); yet the dominance of low-level clouds during ARTofMELT is consistent with the well-
315 established prevalence of LLCs in the central Arctic (Intrieri et al., 2002; Jimenez et al., 2025; Vüllers et al., 2021).

316 The 23 Helikite flights and their respective maximum altitude are displayed in Fig. 3b. Flights covered the full period and
317 sampled all the conditions encountered during the campaign. Clouds were sampled on 8 days with the Helikite (16/23 Helikite
318 flights in total). Out of these 8 cloud situations, the Helikite flew above the cloud top on 5 different days (8 different flights in
319 total). More details on the vertical measurements of these 5 clouds are provided below (Sect. 3.1).

320 The median LWP (Fig. 3c) was 27.9 g m^{-2} during cloudy conditions with an interquartile range (IQR) from 12.3 to 65.1 g m^{-2} .
321 These values are similar to previously reported values from 2.5 years of cloud observations conducted at Ny-Ålesund by
322 Gierens et al. (2020), who observed a median LWP of 24.3 g m^{-2} [IQR = $7.3 - 55.6\text{ g m}^{-2}$] for the summer season, and are to
323 be expected for Arctic clouds (Sedlar, 2014).

324 In Fig. 3d, we can see how the presence of clouds affects the surface radiative budget. The net longwave flux (i.e., downwelling
325 minus upwelling radiation fluxes) shows a bimodal pattern with values $\approx -72\text{ W m}^{-2}$ during clear sky conditions and $\approx -4\text{ W m}^{-2}$
326 during cloudy conditions, which are typical for the Arctic summer (e.g., Solomon et al., 2023). We also assessed the total
327 cloud radiative effect (CRE) by comparing measured downwelling fluxes (both longwave and shortwave) to simulated fluxes
328 with a radiative transfer model assuming clear sky conditions. More details on the data and radiative transfer simulations are
329 provided in the data descriptor (Murto et al., 2024).

330 The total CRE was calculated as,

331

$$332 \text{ CRE} = LW_{\downarrow, \text{measured}} - LW_{\downarrow, \text{clear sky}} + (SW_{\downarrow, \text{measured}} - SW_{\downarrow, \text{clear sky}})(1 - \alpha), \quad (5)$$

333

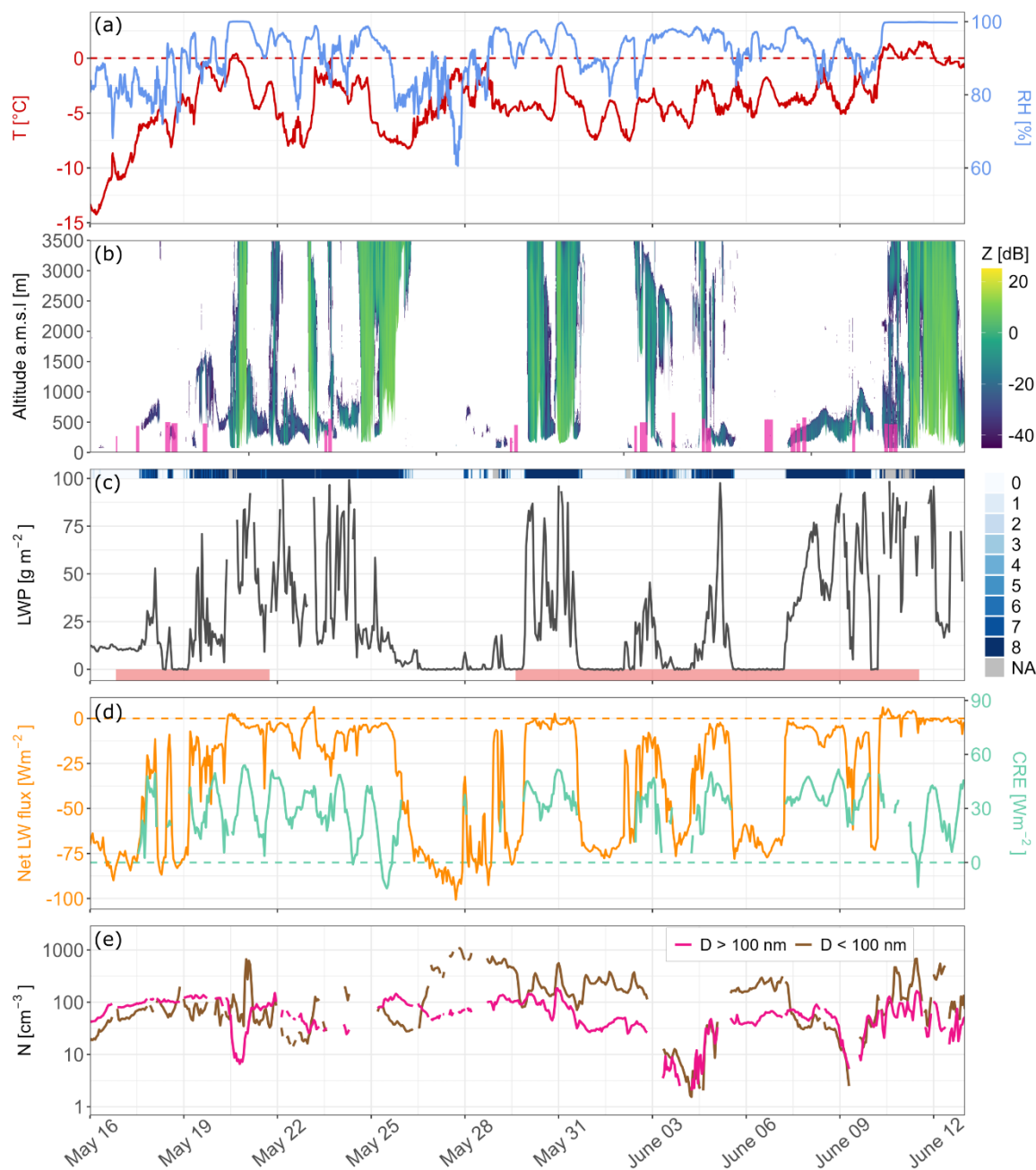
334 where $LW_{\downarrow, \text{measured}}$ and $LW_{\downarrow, \text{clear sky}}$ represent the measured and simulated clear sky downwelling longwave radiation fluxes,
335 respectively. $SW_{\downarrow, \text{measured}}$ and $SW_{\downarrow, \text{clear sky}}$ represent the same but for the shortwave radiation. The α is the surface albedo
336 and was obtained from the on ice weather station measurements. By multiplying the difference in SW_{\downarrow} by $1 - \alpha$, we obtain the



337 difference of absorbed shortwave radiation between clear sky and cloudy conditions. The albedo data was interpolated between
338 the two ice camps to provide a representative value for snow covered ice conditions. Here we assume the LW_{\uparrow} (upwelling
339 longwave radiation) is the same for clear sky and cloudy situation and α is independent of SW_{\downarrow} . The CRE (Fig. 3d) during the
340 campaign was generally positive with maximum values of $\approx 50 \text{ W m}^{-2}$ at local midnight when the sun was at its lowest point.
341 At noon, the CRE was lower but usually remained positive. These observations confirm the warming effect of clouds in the
342 Arctic and their importance for the SEB and sea-ice melt.

343 Figure 3e shows the aerosol concentration measured by the DMPS onboard *IB Oden* for two size ranges ($< 100 \text{ nm}$ for
344 nucleation and Aitken mode particles and $> 100 \text{ nm}$ for accumulation and coarse mode particles). The total concentration
345 varied between a maximum of $\approx 1200 \text{ cm}^{-3}$ and a minimum of below 5 cm^{-3} , while the median was $\approx 170 \text{ cm}^{-3}$. Excluding a
346 few brief interruptions, the first period (until May 25) is marked by a dominance of accumulation mode particles, a signature
347 of Arctic haze, characteristic of spring conditions (e.g., Boyer et al., 2023; Freud et al., 2017; Heutte et al., 2025; Schmale et
348 al., 2022). The median concentrations were 81 and 45 cm^{-3} for particles greater than and smaller than 100 nm, respectively.
349 On May 26, we observe a shift to a summer regime with more dominance of nucleation and Aitken mode particles from local
350 natural sources such as emissions from biological activity (e.g., Leck and Persson, 1996; Pereira Freitas et al., 2025). The
351 respective median concentrations were then 50 and 160 cm^{-3} for particles greater than and smaller than 100 nm.

352
353
354
355



356

357

358

359

360

361

362

363

Figure 3 Overview of cloud relevant variables during the ARTofMELT campaign, May 16 to June 23. (a) Ship-based temperature (red) and relative humidity (blue) measurements 25 m above sea level. Horizontal dashed line indicates 0 °C. (b) Radar reflectivity measurements, up to 3500 m, show the presence of LLCs. Purple rectangles indicate each Helikite flight, including its maximum altitude and duration. (c) Liquid water path (LWP) measured with the HATPRO microwave radiometer. The top bar indicates the cloud fraction in oktas while the lower pink bars indicate the two ice camp periods. (d) Net longwave radiation (orange) and cloud radiative effect (CRE, green). (e) Aerosol particle concentration at ship level for particles with diameters below (brown) and above (pink) 100 nm, respectively. Periods influenced by ship pollution were removed in panel e.



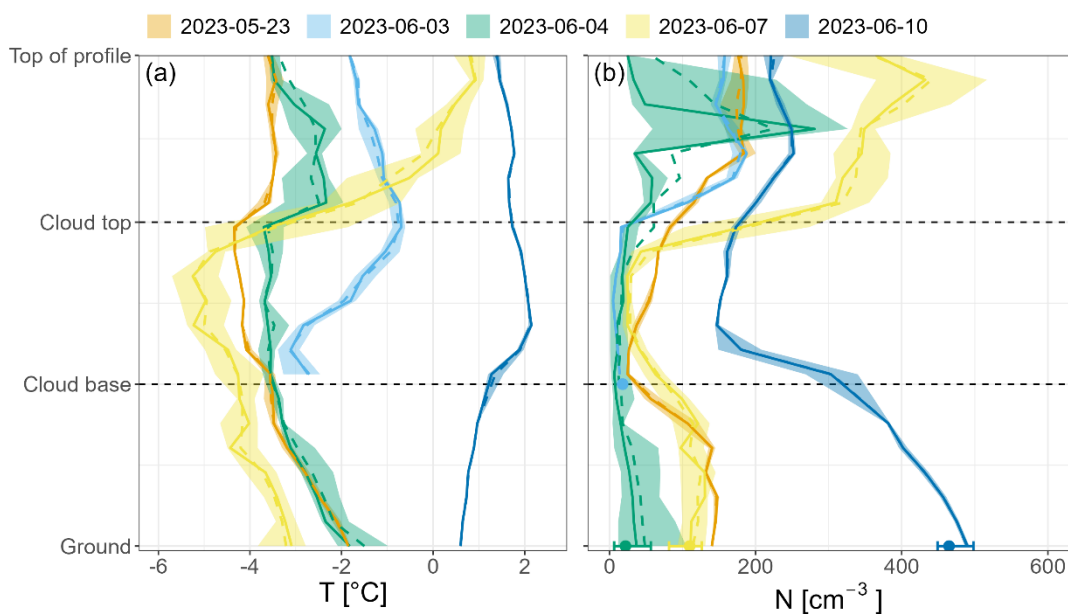
364 **3.1 Diverse aerosol profiles through clouds measured with the Helikite**

365 Here we focus on the five cloud cases where the Helikite flew above the cloud top, allowing aerosol measurements to be
366 collected aloft. Average temperature and aerosol profiles for each case study are shown in Fig. 4. To facilitate comparison
367 across cases, the altitude of each profile was normalized such that the distances between the lowest altitude and cloud base,
368 cloud base and cloud top, and cloud top and the maximum altitude are each mapped onto one third of the profile. The flight
369 on June 3 was conducted in fog; therefore, the profile begins at the cloud base, which coincides with the start altitude.

370 The flights conducted on May 23, June 4, and June 7 exhibited a relatively well mixed boundary layer with no significant
371 aerosol concentration gradients between the surface and cloud base. Measured aerosol concentrations progressively decreased
372 with altitude as the Helikite approached cloud base and reached a minimum inside the cloud, suggesting they were
373 progressively activated with height into cloud droplets over a distance of a few tens of meters and were therefore not sampled
374 by the inlet (as illustrated in Fig. S4). These concentration gradients reflect the diffuse cloud boundaries discussed in Sect. 2.5,
375 where the clouds' optical depth gradually increases along with the number of cloud droplets but is initially below the remote
376 sensing instruments detection limit. The well-mixed boundary layer below the clouds was consistent with the temperature
377 profiles (Fig. 4a), which showed no inversion below the cloud base on any of these days. In contrast, the June 10 flight
378 displayed a pronounced negative aerosol gradient from the surface to the cloud base. On this day, a surface-based temperature
379 inversion due to the advection of a warm air mass was observed, indicating reduced vertical mixing between the surface and
380 the cloud base. This indicates that surface-based measurements were not representative of cloud-level conditions for CCN and
381 INP concentrations at that time.

382 For the June 10 flight, the concentration of interstitial aerosols ($\approx 150 \text{ cm}^{-3}$) was greater than on other days due to increased
383 concentrations of Aitken and nucleation mode particles - too small to activate in this case. Except for June 10, higher aerosol
384 concentrations were observed above the cloud compared to below with enhancement factors between 1.3 and 3.9. These
385 findings are consistent with previous studies (e.g., Kupiszewski et al., 2013; Pilz et al., 2024) underlining the likely relevance
386 of free tropospheric aerosols as an important source of CCN and INPs for Arctic LLCs, which is not captured by surface-based
387 measurements. To further investigate the contribution of particles below and above the cloud to the cloud droplet number
388 concentration and longwave radiative properties, a detailed case study is presented in the following section.

389
390
391



392

393 **Figure 4** Averaged profiles of (a) temperature and (b) aerosol concentrations (for particles with diameters from 8 to 3370 nm)
 394 through low-level clouds or fog layers (dates are indicated in the color legend). The altitude of each profile was normalized to the
 395 altitude of the cloud base and top, such that below, within and above cloud each represent one third of the vertical profile. Full lines
 396 represent the median of all profiles per day, the dashed line is the mean, and the shading represents the interquartile range. Dots
 397 and error bars represent the median and interquartile range from ship-based measurements with the DMPS (15 – 870 nm, no data
 398 on May 23).

399

400 **4 Case study of free tropospheric CCN influence on long-lived low-level mixed phase cloud**

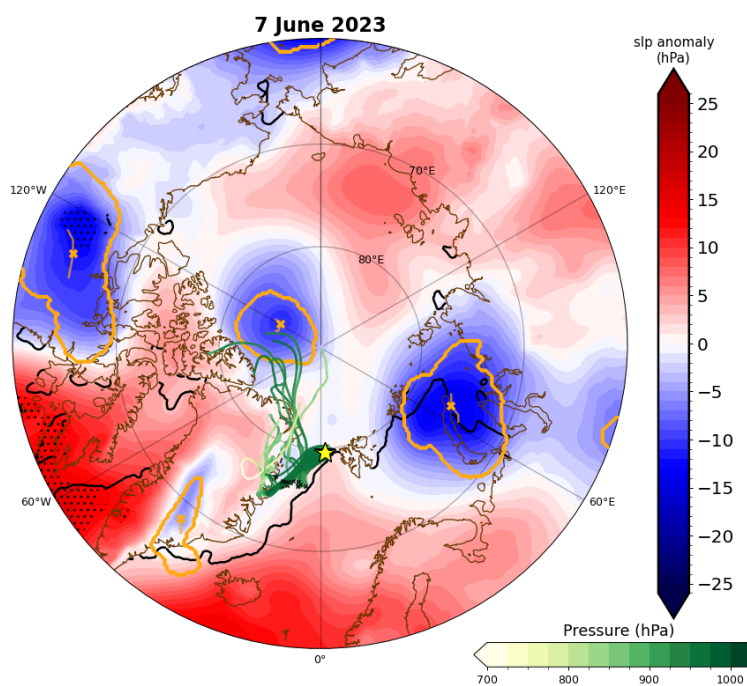
401 On the morning of June 7, 2023, a low-level cloud was advected over the ship location at 79.64°N, 2.52°E. The cloud cover
 402 persisted through the day and continued until late on June 9, allowing several Helikite flights through the cloud to collect
 403 detailed information on aerosol and cloud microphysical characteristics.

404 **4.1 Synoptic conditions and air mass history**

405 In Fig. 5 the sea-level pressure (SLP) anomalies north of 60°N are visualized for June 7, and complemented by five-day back
 406 trajectories arriving at 50 hPa above sea level (\approx cloud height) at the ship location. The SLP anomalies show a low-pressure
 407 trough extending along the East coast of Greenland and high-pressure ridge over the Greenland Sea that extends over the sea
 408 ice. The *Oden* was located at the tip of the ridge. Not seen in Fig. 5 is a cyclone located north of Svalbard between June 2 and
 409 June 5. The back trajectories indicate that the air arriving at *Oden* originated from the central Arctic (north of Greenland) and
 410 followed the trough along the Greenlandic East coast before turning and traveling north towards the ship, along the marginal
 411 ice zone between the low-pressure trough and high-pressure ridge. The arriving air (at the surface) initially travelled in the free



412 troposphere (see vertical cross-sections of trajectories in Fig. S5) and began descending approximately 72 hours before
413 reaching *Oden*, entering the boundary layer ≈ 36 hours before arrival and following the surface for the last 24 hours. The air
414 arriving in the lower troposphere mainly remained in the free troposphere but trajectories show more spread compared to the
415 trajectories arriving at the surface. About half of the trajectories exhibited subsidence over the last 36 hours before reaching
416 *Oden*, which is consistent with the presence of the high-pressure system.
417

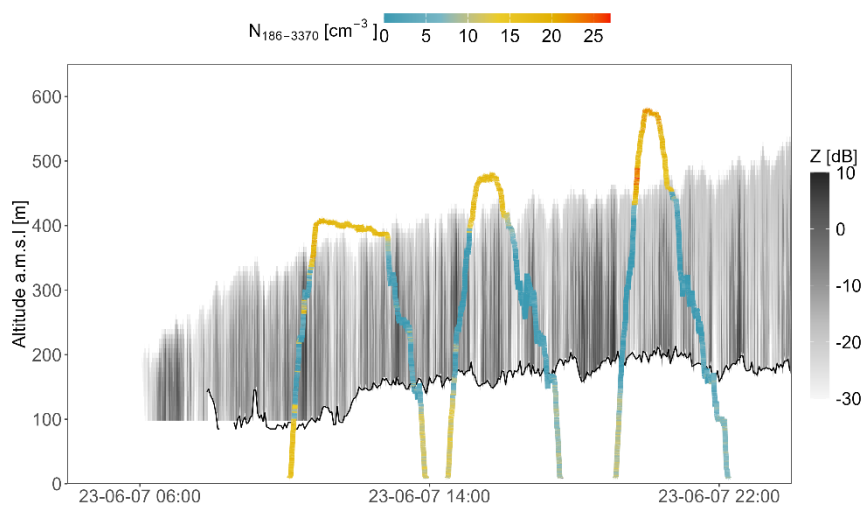


418
419 **Figure 5** Synoptic chart of the northern hemisphere between 60 and 90°N on June 7. Red and blue shading indicate daily-mean sea-
420 level pressure anomalies (hPa) with respect to the climatological mean (May-June 1981-2020; significant anomalies as hatching).
421 Cyclone objects are indicated in orange contours, cyclone tracks in orange thin lines and crosses mark their location at 12 UTC. The
422 thick black contours denote sea ice concentration of 15%. Five-day back trajectories initialized at 12 UTC from the surface (50 hPa
423 AGL) at equidistant spacing of 30 km within a circle (1000 km radius) around the location of *Oden* (yellow star) are shown with
424 green lines (green tone indicates the atmospheric pressure along the air parcels; black crosses show the location at -1d prior to
425 arrival). Significance of anomalies is assessed using a Monte Carlo test: daily means are randomly sampled 1000 times over the
426 climatological period. Daily anomalies exceeding the 5-95th percentile range are considered significant.

427 Figure 6 shows how the cloud developed during the day on June 7. The cloud base was initially very low (< 100 m, which is
428 below the first range gate of the cloud radar). Around 09:00, the cloud base began to rise to approximately 150 m a.s.l. and
429 remained roughly stationary throughout the day. The radar reflectivity indicates that the cloud top increased in altitude
430 throughout the day from ≈ 200 m at 06:00 to ≈ 500 m at the end of the day. Note that a cirrus cloud was detected by the cloud
431 radar around 7 km a.s.l. for the majority of the morning and intermittently during the afternoon (Fig. S6). However, it was not
432 obvious from the photo records of the Helikite camera, indicating that the cirrus was likely optically thin.



433 Light snowfall was observed on the ground throughout the day, indicating that the cloud was a mixed-phase cloud. However,
434 no direct in situ measurements with the Helikite could provide information on the ice water content.
435 Three Helikite flights traversed the cloud between 10:07 and 22:16 UTC. In Fig. 6, the altitude of the Helikite is represented
436 by the colored path, indicative of the measured concentration of aerosols ($N_{186-3370}$). For context, in addition to the apparent
437 depletion inside the cloud due to cloud droplet formation, we observe a decrease in $N_{186-3370}$ at the surface throughout the day,
438 possibly due to scavenging from snowfall and increasing concentrations above the cloud.



439
440 **Figure 6** Time series of the Helikite flight paths as a function of altitude during the three flights on June 7, 2023. The paths are
441 colored according to measured $N_{186-3370}$. Grey shading is the measured radar reflectivity, indicating the cloud's presence. The black
442 line indicates the measured cloud base from the ceilometer.

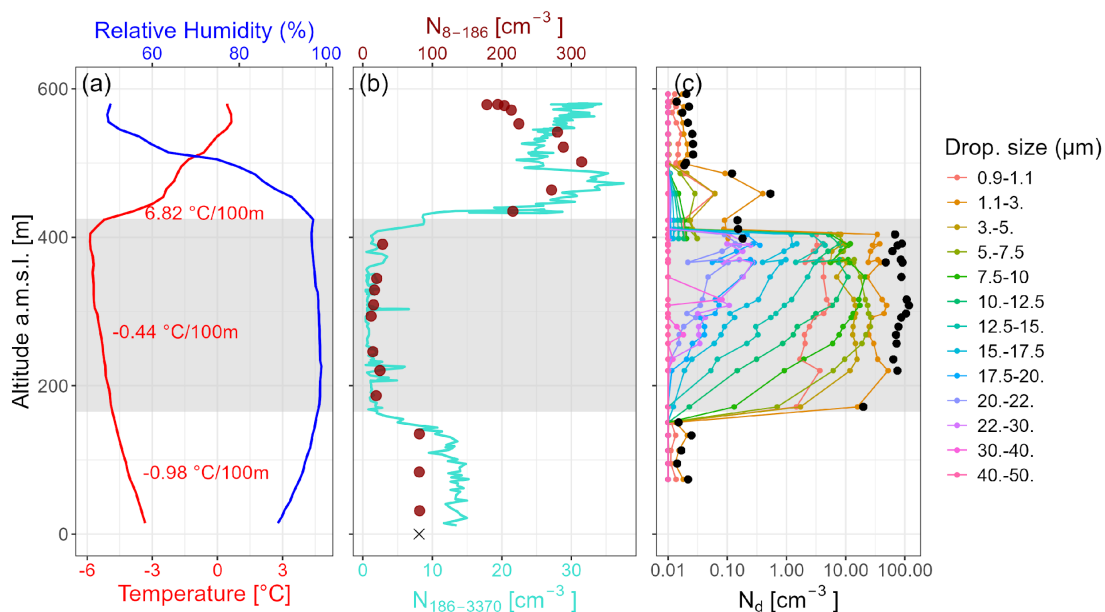
443

444 4.2 Vertical distribution of aerosol properties and cloud droplets

445 Figure 7 shows a snapshot of the atmospheric column during the third ascent of the day (from 19:09 to 20:06 UTC). In Fig.
446 7a, we observe a temperature profile with a dry adiabatic lapse rate below the cloud and wet-adiabatic lapse rate inside the
447 cloud. Starting just below cloud top (≈ 25 m), a temperature inversion marks the transition to the free troposphere and shows
448 the presence of a warm air mass aloft. The temperature below the cloud ranged from -4.8 to -3.3 °C, within the cloud from $-$
449 5.8 to -4.8 °C and above cloud reached as high as $+0.7$ °C. The aerosol profile (N_{8-3370}) indicates an average concentration of
450 ≈ 100 cm^{-3} between the surface and cloud base (Fig. 7b). From about 40 m below cloud, at 125 m, the concentration decreases
451 to reach its minimum at the defined cloud base of 165 m. Inside the cloud, the 10-sec averaged $N_{186-3370}$ does not exceed 6 cm^{-3} .
452 At the top of the cloud, the aerosol concentration increases gradually between 400 and 440 m, while the cloud top was
453 identified at 425 m. This 40-m thick layer corresponds to the entrainment zone (the thin, turbulent layer where dry free
454 tropospheric air mixes into the cloud), located between the boundary layer and the free troposphere. In the free troposphere,



455 the aerosol concentration exceeds the boundary layer concentration with a maximum concentration (N_{8-3370}) of up to about 350
 456 cm^{-3} . The free tropospheric aerosol profile presents, in addition, a layered structure with concentration differences between the
 457 layer in the direct vicinity of the cloud and a layer located above 500 m. Examining the temperature and relative humidity
 458 profiles, we do not identify any major features or differences indicating a separation of air masses that could explain these
 459 observations, besides a small fluctuation in the temperature profile (i.e. slightly stronger temperature gradient) around 500 m.
 460 The profile of cloud droplets (Fig. 7c) shows an increasing number concentration with altitude for all droplets equal to or larger
 461 than $3 \mu\text{m}$. In the upper part of the cloud, N_d is around 100cm^{-3} with a maximum $\approx 130 \text{cm}^{-3}$. Throughout the day, the median
 462 N_d was 88cm^{-3} . Of the measured N_d , 25 % was equal to or higher than 107cm^{-3} and 10 % was equal to or higher than 125cm^{-3} .
 463 Such values are typically on the upper end of cloud droplet number concentrations observed in Arctic LLCs, but are realistic.
 464 For instance, from two years of continuous observations of aerosols and clouds at the Mount Zeppelin Observatory, Koike et
 465 al. (2019) reported a median N_d of 65cm^{-3} between May and July, with a 75th quantile around 110cm^{-3} . In the present context,
 466 these observations indicate that unless all particles from the boundary layer, including nucleation mode sizes were activated,
 467 the aerosol concentrations observed in the boundary layer are not sufficient to provide CCN for all observed cloud droplets.
 468 Thus, a contribution of aerosols from another source (i.e., from above the cloud) is necessary to provide sufficient CCN for
 469 the cloud.



470
 471 **Figure 7** Vertical profiles for the 3rd ascent (19:09 to 20:06 UTC) on June 7 of (a) Temperature (red) and relative humidity (blue)
 472 spatially averaged every 10 m, (b) aerosol number concentration from 8 to 186 nm at a 2 minutes and 40 seconds time resolution
 473 measured with the mSEMS (brick) and 186 to 3370 nm at a 10-sec time resolution measured with the POPS (turquoise), (c) droplet
 474 number concentrations (30-sec resolution) for various sizes and total droplet concentration (black) measured with the LOAC. The
 475 cross on panel (b) represents the mean particle number concentration measured with the DMPS (15 to 870 nm) at ship level during
 476 the profile. The grey shading represents the defined cloud boundaries.

477



478 Based on the observed vertical profile of aerosols, we identified five different layers with distinct aerosol characteristics: the
479 boundary layer, the cloud layer, the cloud-top entrainment zone, the free troposphere in the direct vicinity of the cloud, and
480 above 500 m. The latter was only reached on the last of the three flights and therefore has fewer observations.

481 We extracted the PNSD in each layer for all three Helikite flights from 10:10 to 22:15 UTC. The measured PNSDs are shown
482 in Fig. 8b, while Fig. 8a provides an illustration to help the reader identify which vertical layer is associated with each PNSD.

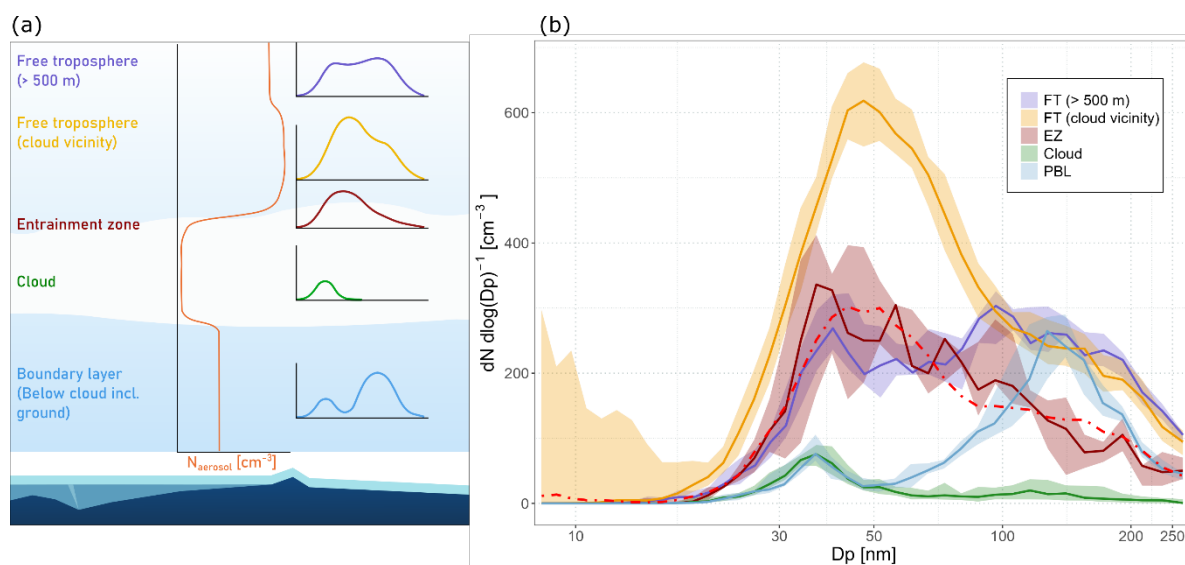
483 Starting from the surface, the boundary layer PNSD (blue) exhibited a bimodal distribution with an Aitken mode peaking at
484 37 nm and a dominant accumulation mode at 125 nm. A distinct Hoppel minimum was located at 52 nm (exact value obtained
485 from a distribution fit), indicating that the boundary layer aerosols have been cloud processed. This distribution was observed
486 from the surface to the cloud base. In the cloud (green), the Aitken mode was identical to that in the boundary layer, but
487 accumulation mode particles were activated into droplets and not sampled. The difference between boundary layer and in-
488 cloud distributions appeared at the Hoppel minimum, indicating activation of particles as small as ≈ 52 nm. The similarity of
489 these size distributions confirms that the cloud was coupled to the surface and that aerosols were well mixed within these two
490 layers. In the entrainment zone, we obtained only five mSEMS scans. These scans were obtained at the cloud top interface, at
491 the base of the temperature inversion, and were identified because of their distinct shape that differed from the cloud and free
492 tropospheric PNSDs. Although quite noisy, we observed an Aitken mode somewhere between 30 and 50 nm. The PNSD
493 extended into an accumulation mode but with no distinct separation between the two modes. In the free troposphere, the PNSD
494 exhibited a different shape compared to the boundary layer. In the lower part (< 500 m), the PNSD was dominated by an
495 Aitken mode with a peak at 47 nm with an accumulation mode shoulder at 130 nm. We also observed a burst of nucleation
496 mode particles during the first flight between 10:50 and 12:50 UTC when the Helikite remained within 50 m of the cloud top.

497 This burst is indicative of new particles being formed in the direct vicinity of cloud top, which could be explained by increased
498 UV irradiance due to the cloud's reflection (Wehner et al., 2015), mixing of dry and wet air in the entrainment zone and
499 potentially a supersaturation of precursor gases that could have been transported in updrafts (Kerminen et al., 2018; Wu et al.,
500 2021). Despite not observing these particles, nor a growth during the subsequent flights, these observations underline the
501 potential of cloud-mediated NPF events in the free troposphere as a source of CCN in the Arctic. Without more detailed
502 information on the composition of the particle precursors and direct observations of a growth event, we cannot speculate on
503 the origin of this event or its impact on the aerosol population. Above 500 m, the PNSD exhibits a different shape from the
504 one below 500 m. Because of limited sampling time, the PNSD looks noisier, but we can identify a similar accumulation mode
505 as seen below 500 m. These particles seem to constitute an older background of the free tropospheric aerosol population.

506 However, we see a smaller Aitken mode and no distinct Hoppel minimum. The reason for the difference between these two
507 free tropospheric layers is not clear. As indicated earlier, we do not observe a distinct indication of a separation of air masses
508 and back trajectory analysis suggests the same origins (Figs. 5 and S6). We can only hypothesize that the layer up to 500 m is
509 more directly influenced by the cloud and the Aitken mode is the result of more recently formed particles directly above the
510 cloud which then grew further.



511 Observations of the PNSD in the boundary layer, cloud, and lower free troposphere tend to indicate that aerosols within the
512 boundary layer - and consequently at the surface - are representative of the population governing cloud microphysical
513 properties. However, the number of observed cloud droplets cannot be explained solely by boundary layer CCN. The integrated
514 aerosol number concentration above the Hoppel minimum (below the cloud) is $\approx 80 \text{ cm}^{-3}$, which represents a gap of $\approx 50 \text{ cm}^{-3}$
515 ± 25 , taking into account uncertainties of N_d measurements) compared to the observed droplet concentration.
516 To understand how significant the contribution from the free troposphere is, we investigate more deeply the interface between
517 the very top of the cloud and the free troposphere, i.e. the entrainment zone. There, the concentration of Aitken mode particles
518 is greater than in the boundary layer but smaller than in the free troposphere, suggesting a mix of free tropospheric and
519 boundary layer air, with some accumulation mode particles that are activated, and hence not sampled. To verify this hypothesis,
520 we computed the mean of the low free troposphere PNSD (yellow) and in-cloud PNSD (green), assuming a one-to-one mixing
521 ratio, and compared it to the entrainment zone PNSD. The resulting PNSD shows a good agreement with the observed PNSD
522 in the entrainment zone (Fig. 8b, red dashed line) strongly supporting the idea that the air from the free troposphere is mixed
523 downwards, contributing to the cloud's CCN population. To further assess the contribution of the entrained air at the top of
524 the cloud, we use a cloud droplet parametrization based on the PNSD measured in the boundary layer and an average of the
525 boundary layer and free tropospheric PNSDs and compare the results to the in situ observations of cloud droplets.
526



527
528 **Figure 8 Particle number size distributions (corrected to standard temperature and pressure) measured in the boundary layer**
529 **(PBL), cloud, entrainment zone (EZ) and free troposphere (FT) in the vicinity of the cloud and above 500 m between 10:10 and 22:15**
530 **UTC on June 7, 2023. The full line represents the median of all distributions and the shading is the interquartile range. The dashed**
531 **red PNSD represents the average of the in-cloud (green) and above cloud (yellow) size distribution.**



532 4.3 Cloud droplet activation parametrization

533 Here we used the methodology introduced in Sect. 2.6 to parametrize the number of droplets in the cloud using two different
534 PNSD inputs. First, we used the boundary layer PNSD, which is in this case representative of the surface measurements. In a
535 second set of parametrizations, we used the average distribution of the boundary layer and lower free tropospheric PNSDs
536 (referred hereafter as EZ PNSD for simplicity), which is a proxy for the total aerosol PNSD in the entrainment zone and
537 represents the cloud-top particle entrainment scenario. We applied the parametrization using the hourly updraft velocity fits
538 from the Doppler Lidar between 10:00 and 23:00 UTC. While this approach is appropriate for a parametrization based on
539 boundary-layer aerosol properties, it represents a simplification for the case including entrainment of aerosols at cloud top. In
540 particular, the vertical velocity and supersaturation conditions near cloud top may differ substantially from those at cloud base,
541 and cloud-top supersaturation can be influenced by different processes than the expansion of air in updrafts, notably by
542 longwave radiative cooling. These processes are not explicitly represented in the present framework. However, due to the lack
543 of direct constraints on cloud-top updrafts and radiatively driven supersaturation, a consistent characteristic velocity based on
544 cloud base measurements is retained for both parametrizations. This limitation should be considered when interpreting the
545 results and highlights the need for future studies to better account for such mechanisms when parametrizing cloud droplet
546 formation in Arctic LLCs.

547 The κ value was calculated as described in Sect. 2.6. Since the value obtained with this method depends on the considered
548 supersaturation, the D_d (i.e. minimum dry diameter of activated particles) in the cloud was estimated from the difference
549 between the in-cloud and boundary layer size distributions. The supersaturation of the cloud was then estimated by
550 interpolating that from the CCNC for the two nearest D_d . The κ value was then calculated using Eq. (2) with the best estimates
551 of D_d and supersaturation (details are shown in Fig. S7).

552 The κ (based on ship-based measurements) was calculated as 0.58 with an uncertainty range from 0.57 to 0.66 corresponding
553 to a supersaturation range between 0.35 and 0.49 %.

554 To account for the uncertainty range in the κ -value and the unknown κ -value of free tropospheric aerosols, we performed a
555 sensitivity analysis with an extended range of values between 0.5 and 0.9. Results indicate no significant difference for each
556 end of the κ -value range for parametrizations with the boundary layer PNSD input. The median N_d ranges from 67 to 70 cm^{-3}
557 (see Fig. S8a). For the parametrizations with the EZ aerosols, results of the sensitivity analysis range between 117 and 130 cm^{-3} .
558

559 Another sensitivity analysis was performed on the characteristic velocity (w^*) where different coefficients of σ were used to
560 account for the uncertainties related to processes controlling the supersaturation in our comparison (see Fig. S8b). We observe
561 a similar behavior as for the sensitivity test on κ -values, where N_d is almost not sensitive to different coefficients of σ for
562 parametrizations with the boundary layer PNSD. For parametrizations with the EZ aerosols, the median ranges from 116 to
563 133 cm^{-3} . Overall, parametrizations with the EZ aerosols show slightly higher sensitivity to κ and w^* but the absolute N_d
564 difference between the two scenarios remains within the same order of magnitude (i.e., a difference ranging between ≈ 50 to

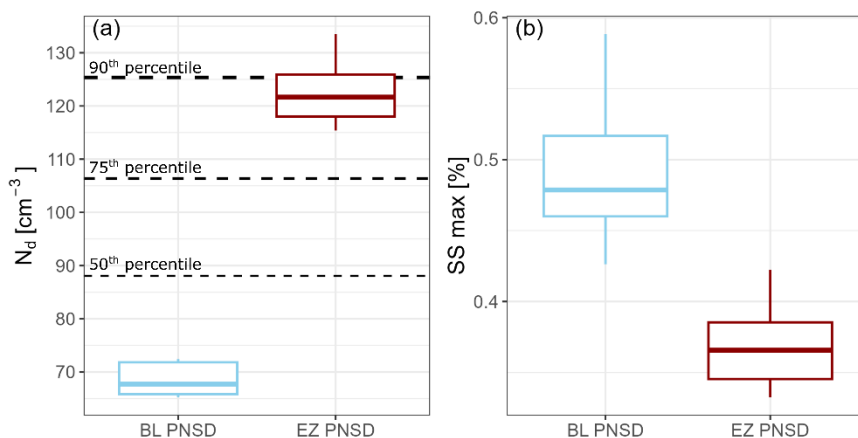


565 60 cm⁻³). The higher sensitivity to κ and w^* suggests that with the contribution of free tropospheric CCN, the cloud was in an
 566 updraft-limited regime but if we only consider the boundary layer aerosols, the number of cloud droplets would be more limited
 567 by the availability of CCN within the tested range of κ and w^* as an increase in the updraft velocity or κ did not lead to an
 568 increase in N_d (or is only limited).

569 In Fig. 9, we see results of (a) N_d and (b) maximum supersaturation (ss_{max}) for parametrizations with a κ of 0.58 and $w^* = 0.79\sigma$
 570 (center estimates). The median N_d for boundary layer and EZ aerosols is 68 and 122 cm⁻³, respectively, which represents an
 571 increase of 80 % for the EZ scenario. The ss_{max} is lower for the parametrization with EZ aerosols, because of the higher number
 572 of CCN but the values remain similar to the estimated ss_{max} range from the κ -value calculations (see Fig. S8).

573 The N_d results from the parametrization show a very good agreement between the EZ scenario and the in situ observations
 574 with concentrations around 100 cm⁻³ and occasionally over 130 cm⁻³ (Fig. 7). This confirms the significant influence of
 575 entrained free tropospheric aerosols on the cloud's microphysics.

576



577

578 **Figure 9 (a) Boxplot of droplet numbers from the aerosol activation parametrization using the boundary layer PNSD (blue) and**
 579 **entrainment zone PNSD (dark red) as inputs. The horizontal dashed lines represent the 50th, 75th and 90th percentiles of cloud droplet**
 580 **concentrations observed with the LOAC. (b) Parametrized maximum supersaturation with the two different PNSD inputs. The**
 581 **boxplots represent the median and interquartile range, the whiskers' length equals to 1.5 times the interquartile range.**

582 4.4 Influence of the free tropospheric aerosols on the cloud longwave radiative forcing

583 The longwave radiative absorption, re-emission and transmission through a cloud are a function of the cloud's optical depth,
 584 cloud phase, droplet size and emitting temperature (Stephens, 1978). The longwave flux follows the Stefan-Boltzmann
 585 relationship:

$$586 F = \varepsilon\sigma T^4, \tag{6}$$

587 where F is the radiation flux, ε is the apparent emissivity, σ ($5.67 \times 10^{-8} \text{ W m}^{-2} \text{ K}^{-4}$) is the Stefan-Boltzmann constant and T is
 588 the emitting temperature in Kelvin. The emissivity is a function of the longwave optical depth and is often specified as a
 589 function of the LWP,



590 $\varepsilon = 1 - e^{(-a_0 LWP)},$ (7)

591 wherein a_0 ($\text{m}^2 \text{g}^{-1}$) is the mass-absorption coefficient (Stephens, 1978). For a cloud with a LWP between roughly 30 to 50 g
592 m^{-2} , the emissivity approaches unity (Shupe and Intrieri, 2004). Although it is not explicitly included in Eq. (7), the effective
593 radius of cloud droplets can alter emissivity for non-opaque clouds (Garrett et al., 2002; Garrett and Zhao, 2006). This effect
594 has been found to be negligible at the global scale (Rotstajn and Penner, 2001) but observations suggest that the effect can be
595 significant for Arctic clouds where the longwave warming effect is dominant and where CCN concentrations are typically
596 orders of magnitude lower than in the midlatitudes (e.g., Curry and Herman, 1985; Garrett et al., 2002; Garrett and Zhao,
597 2006).

598 Here, we use idealized RTM to examine how additional CCN originating from the free troposphere modify the cloud's
599 emissivity and surface longwave radiative forcing through their impact on cloud droplet number concentrations (c.f. Sect. 2.7).
600 We focus on the longwave part of the radiation spectrum to specifically evaluate the difference in emissivity for different N_d .
601 Simulations were performed omitting the ice phase since we do not have direct measurements of the ice water content and
602 because the longwave emissions are largely dominated by the liquid droplets (Curry et al., 1993; Hofer et al., 2024).

603 The RTM simulation was run using data at 11:30 and 17:30 UTC (radiosonde launches) with LWPs for the first and second
604 profiles of 26.2 g m^{-2} and 37.9 g m^{-2} , respectively. Fig. 10a shows results of longwave radiative forcing for simulations with
605 different cloud droplet number concentration profiles. The longwave forcing was determined by computing the difference in
606 downwelling longwave radiation ($LW \downarrow$) between cloudy conditions and a cloud-free (cloud was removed) scenario. The
607 cloud's microphysical properties were based on the N_d parametrization outputs from Sect. 4.3 (located on each side of the grey
608 stripe in Fig. 10), representing a scenario with and without free tropospheric CCN contribution. We also extended the
609 simulation to lower and higher N_d to create broader context for the interpretation of the results. The r_{eff} profiles typically
610 increase with height inside the cloud because of the increase in LWC near cloud top.

611 The r_{eff} values at cloud base are around $1 \mu\text{m}$ and range between $\approx 5 \mu\text{m}$ and $18 \mu\text{m}$ at cloud top. for profiles with the lowest
612 and highest N_d , respectively. An example of the corresponding r_{eff} profiles for the data at 11:30 UTC is shown in Fig. S9.
613 Results from the RTM remain within 10 W m^{-2} from surface-based observations on the ice, an uncertainty which is to be
614 expected for such simulations (Lonardi et al., 2024; Mauritsen et al., 2011). Because of these uncertainties, our analysis focuses
615 mainly on the absolute difference between the various simulations, and we do not use the observations to directly validate the
616 simulated values.

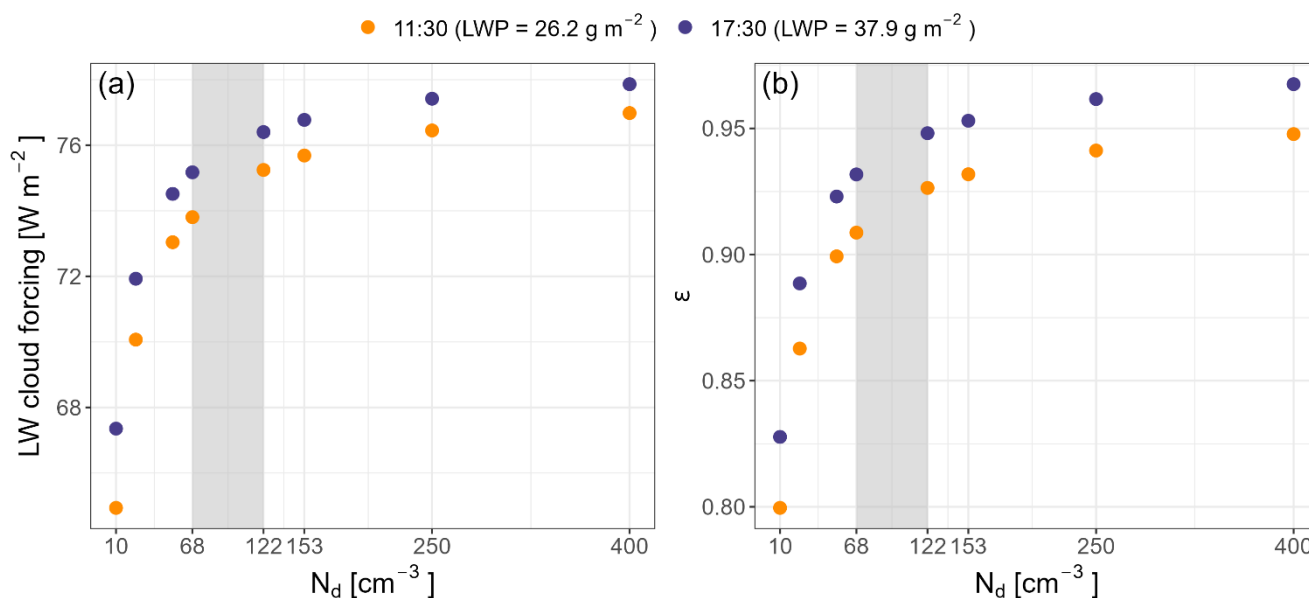
617 The average difference for simulations with $N_d = 68$ and 122 is equal to 1.3 W m^{-2} . This difference accounts for $\approx 2 \%$ of the
618 longwave cloud forcing in this range of N_d (and measured LWP). By rearranging Eq. (6), we can calculate the cloud's apparent
619 emissivity from the longwave radiation results. Apparent emissivity values are generally high (between 0.89 and 0.95 for N_d
620 $\in [68, 122]$) and Fig. 10b shows that the emissivity is slightly higher for the later profile (dark blue points), which is consistent
621 with the increase in LWP between 11:30 and 17:30 UTC.

622 To put these results in perspective, we compare them to the study of Garrett and Zhao (2006) who performed a similar analysis
623 but compared clouds affected by local anthropogenic pollution to clouds formed in clean background conditions over four



624 years of observations at Utqiagvik (Alaska). They reported increased longwave radiative forcing between 3.3 and 5.2 W m⁻²
 625 due to the increased cloud droplet concentrations when clouds were affected by pollution. They reported an average N_d of 53
 626 cm⁻³ and a LWP of 31.1 g m⁻² for clean conditions and 153 cm⁻³ and 33.5 g m⁻² for polluted conditions. While the LWP is
 627 similar to the LWP of our case study, the observed increase of droplets is larger in their study (≈ 3 times more droplets between
 628 the two scenarios). We performed additional simulations with $N_d = 53$ and 153 cm⁻³ to compare our case study with their results
 629 and observe an increase in the cloud's longwave radiative forcing between 2.5 and 3.4 W m⁻². The similarity of our results
 630 indicates that the influence of free tropospheric CCN sources on Arctic cloud radiative properties may be as important as the
 631 perturbations from local anthropogenic sources.

632 Further examining the simulations with even fewer or more droplets, i.e. beyond the grey bar in Fig. 10a, we find that the
 633 cloud's emissivity and radiative forcing exhibit the greatest sensitivity to N_d for values at low concentrations ($< \approx 70$ cm⁻³). As
 634 the concentration increases, the emissivity tends to approach a maximum for the given LWP and cloud's temperature.
 635 Conditions with low aerosol concentration (< 100 or even < 10 cm⁻³) are commonly observed in the central Arctic year-round
 636 (e.g., Bigg et al., 1996; Boyer et al., 2023; Lannefors et al., 1983). Hence, under those conditions, the impact on the radiative
 637 properties of a cloud from the presence of enhanced aerosol layers located above becomes important and model representations
 638 of clouds based on surface-based measurements will lead to a negative longwave forcing bias. This is especially true for clouds
 639 with low LWP, e.g., during foggy conditions in the marginal ice zone and in summer and fall over the sea ice. For reference,
 640 during ARTofMELT, 50% of the measurements indicated a LWP below 27.9 g m⁻² and 25% below 12.3 g m⁻². It is important
 641 to note, however, that while higher aerosol concentrations above the boundary layer/cloud-top are likely common, they are not
 642 universal and concentrations might also be lower.



643
 644 **Figure 10 (a) Simulated longwave cloud forcing at the surface as a function of cloud droplet number concentration for the radiosonde**
 645 **of 11:30 (dark yellow points) and 17:30 (dark blue points) on June 7th, 2023. (b) Calculated cloud's emissivity for different cloud**



646 **droplet profiles. The grey shaded region helps to identify and compare results of cloud droplet number concentration from the**
647 **parametrization presented and discussed in Sect. 4.3.**

648 **5 Conclusions**

649 This study has examined vertical in situ measurements of particle number size distributions, cloud droplets number
650 concentrations and meteorological variables collected with an instrumented Helikite from the icebreaker *Oden* between May
651 16 and June 10, 2023, as part of the ARTofMELT expedition. The primary objective was to evaluate the importance of free
652 tropospheric aerosol sources to form and sustain Arctic LLCs and see to what extent the entrainment of these particles could
653 impact the microphysical and radiative properties of the clouds.

654 In total, five clouds were profiled up to and above their tops, allowing for observations of particle number size distributions
655 below, within, and above the clouds. Four of the five cases indicated enhanced aerosol concentrations above the cloud, which
656 is consistent with previous observations in the Arctic and illustrates the importance of considering elevated aerosol sources for
657 forming and sustaining clouds.

658 We selected a cloud observed on June 7th for a detailed case study. The analysis revealed a complex vertically-layered aerosol
659 structure with several distinct particle size distributions. Starting from the surface, we observed a relatively constant
660 concentration profile, with characteristics of cloud processing, up to the cloud base. Inside the cloud, the interstitial fraction of
661 these aerosols was measured, indicating mixing between the surface and the cloud. Above the cloud, an aerosol population
662 with concentrations 2 to 3 times greater than below the cloud was observed, extending about 100 m above the cloud top. The
663 PNSD was dominated by an Aitken mode but no Hoppel minimum indicating the absence of recent cloud processing. At the
664 cloud top, between free tropospheric and cloud air, we observed a size distribution corresponding to a mixture of the in-cloud
665 and above-cloud PNSDs, indicating that the two air masses from above and within the cloud were mixed, entraining free
666 tropospheric aerosols into the cloud. The analysis of the cloud microphysical properties indicated that the aerosol particles
667 measured in the boundary layer did not constitute a sufficiently large source of CCN to form the observed amount of cloud
668 droplets, requiring an additional source from the free troposphere.

669 The impact of the free-tropospheric source was evaluated using an aerosol activation parameterization based on the PNSDs
670 measured in the boundary layer and in the entrainment zone. Parameterizations including aerosols from the free troposphere in
671 addition to from the boundary layer produced 80% more cloud droplets than parameterizations based solely on boundary-layer
672 aerosols, matching the in situ observations of N_d and confirming the significant contribution of the free tropospheric CCN
673 source. Hence, while the cloud was coupled to the surface and aerosols were well-mixed throughout the boundary layer,
674 measurements at the surface only captured particles that had been processed in the cloud and the information on the entrainment
675 of a different aerosol population at cloud top could not be obtained from those surface-based measurements.

676 Radiative transfer modeling indicated a marginal increase in surface cloud longwave radiative forcing for a scenario where the
677 effect of entrained aerosols at cloud top on the cloud droplet concentration was considered ($\approx 2\%$ of the total surface longwave
678 radiative forcing). However, extended simulations with different cloud droplet number concentrations showed a higher



679 sensitivity of the longwave radiative forcing at low N_d ($< 70 \text{ cm}^{-3}$). Results from these simulations suggest that under conditions
680 where near-surface aerosol concentrations are low (e.g., $< 100 \text{ cm}^{-3}$ or even $< 10 \text{ cm}^{-3}$, including also non-activating particles),
681 aerosol above cloud top can have a significant impact on cloud radiative properties and model representations based on surface-
682 based measurements might lead to significant biases with respect to cloud radiative forcing. In addition, while we kept the
683 LWP constant for all simulations, a lower LWP will generally make a cloud more sensitive to N_d , which means that the free
684 troposphere as source of aerosols really matters.

685 More generally, while the results of this study are based on a limited amount of data, our findings demonstrate that above the
686 sea ice, where aerosol sources can often be limited, aerosols above clouds can constitute a significant source of CCN and INPs
687 and their entrainment is important to consider. It is also important to note that our study presents limitations regarding the
688 simulation of supersaturation conditions at cloud top but a sensitivity analysis of the cloud's characteristic updraft velocity
689 (which drives the supersaturation in the cloud) indicates that our conclusions hold true even for different supersaturations.
690 These limitations should hence be considered for the improvement of Arctic LLCs in models, which should consider sources
691 aloft and the entrainment mechanisms into the cloud, from above.

692 Here, we focused on the number of cloud droplets and their effective radius and how they affected the cloud longwave radiative
693 forcing. To obtain a complete understanding of the role of free tropospheric aerosols on Arctic LLCs, future studies should
694 also focus on how the total condensate and the phase partitioning of clouds are affected and consequently their total radiative
695 forcing and lifetime. More observations combining radiation measurements and detailed in situ aerosol measurements
696 including INPs and cloud microphysical properties (i.e., cloud droplets and ice crystals) are essential to improve our process
697 understanding of Arctic mixed-phase clouds and their representation in models.

698

699 **Data availability**

700 All datasets used in this study can be accessed on the Bolin Centre for Climate Research database following this link:
701 <https://bolin.su.se/data/oden-artofmelt-2023/>. The individual DOI entries are listed here.

702 Tethered-balloon vertical in situ measurements: <https://doi.org/10.17043/oden-artofmelt-2023-aerosols-vertical-1>

703 Ship-based aerosol measurements: <https://doi.org/10.17043/oden-artofmelt-2023-aerosol-source-samples-1>

704 Radiosonde profiles: <https://doi.org/10.17043/oden-artofmelt-2023-radiosonde-1>

705 Cloud radar data: <https://doi.org/10.17043/oden-artofmelt-2023-cloud-radar-1>

706 Ceilometer cloud base heights: <https://doi.org/10.17043/oden-artofmelt-2023-ceilometer-cloudnetpy-1>

707 Halo lidar: <https://doi.org/10.17043/oden-artofmelt-2023-halo-lidar-1>

708 Ice-station meteorological measurements: <https://doi.org/10.17043/oden-artofmelt-2023-surface-meteorology-ice-station-1>

709 Ship-based meteorological measurements: <https://doi.org/10.17043/oden-artofmelt-2023-weather-station-1>

710 Backward trajectory data: <https://doi.org/10.17043/oden-artofmelt-2023-trajectories-backward-circle-1>

711 The data from the LOAC and from the ship-based DMPS can be obtained upon request by contacting the author and is currently
712 being prepared for publication on the Bolin data Centre.



713

714 **Authors contributions**

715 RP: Measurements, data curation and analysis, manuscript original writing. JS: Principal investigator, supervision of the study,
716 data interpretation and manuscript editing. RC contributed to the data processing. LH, IB, HG and NF participated in the
717 deployment of the Helikite. IB and HG conducted remote sensing measurements and provided the data. JK, LH and PZ
718 conducted ship-based aerosol and LOAC measurements and provided the data. SM provided LAGRANTO back trajectories
719 and produced figures for the analysis of the synoptic situation. ML helped with the radiative transfer simulations. All co-
720 authors commented on the manuscript drafts and contributed to the interpretation of the results.

721

722 **Competing interests**

723 At least one of the (co-)authors is a member of the editorial board of Atmospheric Chemistry and Physics.

724

725 **Acknowledgements**

726 This work is part of the ARTofMELT (Atmospheric Rivers and the onset of sea ice MELT) project. The ARTofMELT
727 expedition was supported and organized by the Swedish Polar Research Secretariat (SPRS) on the Swedish research icebreaker
728 *Oden* in spring 2023 under the SWEDARCTIC program. RP and JS received funding from the Swiss National Science
729 Foundation (grant no. 200021_212101). Support also came from the Swedish Council for Research Infrastructures (grant no.
730 2021-00153), the Knut and Alice Wallenberg Foundation (grant no. 2016-0024), the Natural Environment Research Council
731 UK (grant no. NE/X000087/1), U.S. National Science Foundation (grant no. OPP-2226864). This project has also received
732 funding from the European Union's Horizon 2020 research and innovation program under grant agreement No. 101003826 via
733 project CRiceS (Climate Relevant interactions and feedbacks: the key role of sea ice and Snow in the polar and global climate
734 system) and the European Research Council (Consolidator grant INTEGRATE No. 865799). Funding for RC was additionally
735 provided by the European Union's Horizon Europe project “CleanCloud” (Grant agreement No. 101137639). Further funding
736 was provided by the Carl Tryggers Foundation (CTS 22:2148 and CTS 24:03137), Ymer-80-foundation, the Bolin Centre for
737 Climate Research (RA2) and the Ivar Bendixsons scholarship. EST and NF were supported by the Swedish Research Council
738 VR (grant no. 2020-03497). EST and NF contribute to the Strategic Research Area “Modelling the Regional and Global Earth
739 system”, MERGE, funded by the Swedish government.

740 The Doppler lidar were provided by the UK National Centre for Atmospheric Science (NCAS) Atmospheric Measurement and
741 Observation Facility (AMOF).

742 The authors are grateful to the SPRS coordinator Åsa Lindgren and the SPRS support team and to Captain Mattias Petersson
743 and the crew on *Oden*. The authors would also like to thank Anaïs Bretones for her help with the Helikite operations. The
744 authors also thank Lars Aue (AWI Bremerhaven) for providing data for the cyclone tracks and objects. Julia Schmale holds
745 the Ingvar Kamprad Chair for Extreme Environments Research sponsored by Ferring Pharmaceuticals.

746

747



748 **References**

- 749 Achtert, P., Seelig, T., Wallentin, G., Ickes, L., Shupe, M. D., Hoose, C., and Tesche, M.: Occurrence of seeding multi-layer
750 clouds in the Arctic from ground-based observations, *EGUsphere*, 1–29, <https://doi.org/10.5194/egusphere-2025-3529>, 2025.
- 751 Akansu, E. F., Dahlke, S., Siebert, H., and Wendisch, M.: Evaluation of methods to determine the surface mixing layer height
752 of the atmospheric boundary layer in the central Arctic during polar night and transition to polar day in cloudless and cloudy
753 conditions, *Atmos. Chem. Phys.*, 23, 15473–15489, <https://doi.org/10.5194/acp-23-15473-2023>, 2023.
- 754 Barahona, D., West, R. E. L., Stier, P., Romakkaniemi, S., Kokkola, H., and Nenes, A.: Comprehensively accounting for the
755 effect of giant CCN in cloud activation parameterizations, *Atmospheric Chemistry and Physics*, 10, 2467–2473,
756 <https://doi.org/10.5194/acp-10-2467-2010>, 2010.
- 757 Bigg, E. K., Leck, C., and Nilsson, E. D.: Sudden changes in arctic atmospheric aerosol concentrations during summer and
758 autumn, *Tellus B*, 48, 254–271, <https://doi.org/10.1034/j.1600-0889.1996.t01-1-00009.x>, 1996.
- 759 Boyer, M., Aliaga, D., Pernov, J. B., Angot, H., Quéléver, L. L. J., Dada, L., Heutte, B., Dall’Osto, M., Beddows, D. C. S.,
760 Brasseur, Z., Beck, I., Bucci, S., Duetsch, M., Stohl, A., Laurila, T., Asmi, E., Massling, A., Thomas, D. C., Nøjgaard, J. K.,
761 Chan, T., Sharma, S., Tunved, P., Krejci, R., Hansson, H. C., Bianchi, F., Lehtipalo, K., Wiedensohler, A., Weinhold, K.,
762 Kulmala, M., Petäjä, T., Sipilä, M., Schmale, J., and Jokinen, T.: A full year of aerosol size distribution data from the central
763 Arctic under an extreme positive Arctic Oscillation: insights from the Multidisciplinary drifting Observatory for the Study of
764 Arctic Climate (MOSAIC) expedition, *Atmos. Chem. Phys.*, 23, 389–415, <https://doi.org/10.5194/acp-23-389-2023>, 2023.
- 765 Bradley, R. S., Keimig, F. T., and Diaz, H. F.: Climatology of surface-based inversions in the North American Arctic, *J.*
766 *Geophys. Res. Atmos.*, 97, 15699–15712, <https://doi.org/10.1029/92JD01451>, 1992.
- 767 Brenguier, J.-L., Burnet, F., and Geoffroy, O.: Cloud optical thickness and liquid water path – does the k coefficient vary with
768 droplet concentration?, *Atmospheric Chemistry and Physics*, 11, 9771–9786, <https://doi.org/10.5194/acp-11-9771-2011>, 2011.
- 769 Brooks, I. M., Tjernström, M., Persson, P. O. G., Shupe, M. D., Atkinson, R. A., Canut, G., Birch, C. E., Mauritsen, T., Sedlar,
770 J., and Brooks, B. J.: The Turbulent Structure of the Arctic Summer Boundary Layer During The Arctic Summer Cloud-Ocean
771 Study, *J. Geophys. Res. Atmos.*, 122, 9685–9704, <https://doi.org/https://doi.org/10.1002/2017JD027234>, 2017.
- 772 Conant, W. C., VanReken, T. M., Rissman, T. A., Varutbangkul, V., Jonsson, H. H., Nenes, A., Jimenez, J. L., Delia, A. E.,
773 Bahreini, R., Roberts, G. C., Flagan, R. C., and Seinfeld, J. H.: Aerosol–cloud drop concentration closure in warm cumulus, *J.*
774 *Geophys. Res.*, 109, 2003JD004324, <https://doi.org/10.1029/2003JD004324>, 2004.



- 775 Creamean, J. M., de Boer, G., Telg, H., Mei, F., Dexheimer, D., Shupe, M. D., Solomon, A., and McComiskey, A.: Assessing
776 the vertical structure of Arctic aerosols using balloon-borne measurements, *Atmos. Chem. Phys.*, 21, 1737–1757,
777 <https://doi.org/10.5194/acp-21-1737-2021>, 2021.
- 778 Creamean, J. M., Barry, K., Hill, T. C. J., Hume, C., DeMott, P. J., Shupe, M. D., Dahlke, S., Willmes, S., Schmale, J., Beck,
779 I., Hoppe, C. J. M., Fong, A., Chamberlain, E., Bowman, J., Scharien, R., and Persson, O.: Annual cycle observations of
780 aerosols capable of ice formation in central Arctic clouds, *Nat Commun*, 13, 3537, [https://doi.org/10.1038/s41467-022-31182-](https://doi.org/10.1038/s41467-022-31182-x)
781 [x](https://doi.org/10.1038/s41467-022-31182-x), 2022.
- 782 Curry, J. A. and Herman, G. F.: Infrared radiative properties of summertime Arctic stratus clouds, *Journal of Applied*
783 *Meteorology and Climatology*, 24, 525–538, [https://doi.org/10.1175/1520-0450\(1985\)024%3C0525:IRPOSA%3E2.0.CO;2](https://doi.org/10.1175/1520-0450(1985)024%3C0525:IRPOSA%3E2.0.CO;2),
784 1985.
- 785 Curry, J. A., Schramm, J. L., and Ebert, E. E.: Impact of clouds on the surface radiation balance of the Arctic Ocean, *Meteorol.*
786 *Atmos. Phys.*, 51, 197–217, <https://doi.org/10.1007/BF01030494>, 1993.
- 787 Emde, C., Buras-Schnell, R., Kylling, A., Mayer, B., Gasteiger, J., Hamann, U., Kylling, J., Richter, B., Pause, C., Dowling,
788 T., and Bugliaro, L.: The libRadtran software package for radiative transfer calculations (version 2.0.1), *Geosci. Model Dev.*,
789 9, 1647–1672, <https://doi.org/10.5194/gmd-9-1647-2016>, 2016.
- 790 Fan, J., Wang, Y., Rosenfeld, D., and Liu, X.: Review of Aerosol–Cloud Interactions: Mechanisms, Significance, and
791 Challenges, *J. Atmos. Sci.*, 73, 4221–4252, <https://doi.org/10.1175/JAS-D-16-0037.1>, 2016.
- 792 Fountoukis, C. and Nenes, A.: Continued development of a cloud droplet formation parameterization for global climate
793 models, *J. Geophys. Res.*, 110, 2004JD005591, <https://doi.org/10.1029/2004JD005591>, 2005.
- 794 Fountoukis, C., Nenes, A., Meskhidze, N., Bahreini, R., Conant, W. C., Jonsson, H., Murphy, S., Sorooshian, A.,
795 Varutbangkul, V., Brechtel, F., Flagan, R. C., and Seinfeld, J. H.: Aerosol–cloud drop concentration closure for clouds sampled
796 during the International Consortium for Atmospheric Research on Transport and Transformation 2004 campaign, *Journal of*
797 *Geophysical Research: Atmospheres*, 112, <https://doi.org/10.1029/2006JD007272>, 2007.
- 798 Freud, E., Krejci, R., Tunved, P., Leaitch, R., Nguyen, Q. T., Massling, A., Skov, H., and Barrie, L.: Pan-Arctic aerosol number
799 size distributions: seasonality and transport patterns, *Atmos. Chem. Phys.*, 17, 8101–8128, [https://doi.org/10.5194/acp-17-](https://doi.org/10.5194/acp-17-8101-2017)
800 [8101-2017](https://doi.org/10.5194/acp-17-8101-2017), 2017.
- 801 Garrett, T. J. and Zhao, C.: Increased Arctic cloud longwave emissivity associated with pollution from mid-latitudes, *Nature*,
802 440, 787–789, <https://doi.org/10.1038/nature04636>, 2006.



- 803 Garrett, T. J., Radke, L. F., and Hobbs, P. V.: Aerosol Effects on Cloud Emissivity and Surface Longwave Heating in the
804 Arctic, *Journal of the Atmospheric Sciences*, 59, 769–778, [https://doi.org/10.1175/1520-0469\(2002\)059%3C0769:AEOCEA%3E2.0.CO;2](https://doi.org/10.1175/1520-0469(2002)059%3C0769:AEOCEA%3E2.0.CO;2), 2002.
- 806 Georgakaki, P., Bougiatioti, A., Wieder, J., Mignani, C., Ramelli, F., Kanji, Z. A., Henneberger, J., Hervo, M., Berne, A.,
807 Lohmann, U., and Nenes, A.: On the drivers of droplet variability in alpine mixed-phase clouds, *Atmos. Chem. Phys.*, 21,
808 10993–11012, <https://doi.org/10.5194/acp-21-10993-2021>, 2021.
- 809 Gierens, R., Kneifel, S., Shupe, M. D., Ebell, K., Maturilli, M., and Löhnert, U.: Low-level mixed-phase clouds in a complex
810 Arctic environment, *Atmospheric Chemistry and Physics*, 20, 3459–3481, <https://doi.org/10.5194/acp-20-3459-2020>, 2020.
- 811 Heutte, B., Bergner, N., Angot, H., Pernov, J. B., Dada, L., Mirrielees, J. A., Beck, I., Baccarini, A., Boyer, M., Creamean, J.
812 M., Daellenbach, K. R., El Haddad, I., Frey, M. M., Henning, S., Laurila, T., Moschos, V., Petäjä, T., Pratt, K. A., Quéléver,
813 L. L. J., Shupe, M. D., Zieger, P., Jokinen, T., and Schmale, J.: Observations of high-time-resolution and size-resolved aerosol
814 chemical composition and microphysics in the central Arctic: implications for climate-relevant particle properties,
815 *Atmospheric Chemistry and Physics*, 25, 2207–2241, <https://doi.org/10.5194/acp-25-2207-2025>, 2025.
- 816 Hofer, S., Hahn, L. C., Shaw, J. K., McGraw, Z. S., Bruno, O., Hellmuth, F., Pietschnig, M., Mostue, I. A., David, R. O.,
817 Carlsen, T., and Storelvmo, T.: Realistic representation of mixed-phase clouds increases projected climate warming, *Commun
818 Earth Environ*, 5, 390, <https://doi.org/10.1038/s43247-024-01524-2>, 2024.
- 819 Igel, A. L., Ekman, A. M. L., Leck, C., Tjernström, M., Savre, J., and Sedlar, J.: The free troposphere as a potential source of
820 arctic boundary layer aerosol particles, *Geophys. Res. Lett.*, 44, 7053–7060,
821 <https://doi.org/https://doi.org/10.1002/2017GL073808>, 2017.
- 822 Illingworth, A. J., Hogan, R. J., O’Connor, E. J., Bouniol, D., Brooks, M. E., Delanoé, J., Donovan, D. P., Eastment, J. D.,
823 Gaussiat, N., Goddard, J. W. F., Haeffelin, M., Baltink, H. K., Krasnov, O. A., Pelon, J., Piriou, J.-M., Protat, A., Russchenberg,
824 H. W. J., Seifert, A., Tompkins, A. M., Zadelhoff, G.-J. van, Vinit, F., Willén, U., Wilson, D. R., and Wrench, C. L.: Cloudnet:
825 Continuous Evaluation of Cloud Profiles in Seven Operational Models Using Ground-Based Observations, *Bulletin of the
826 American Meteorological Society*, 88, 883–898, <https://doi.org/10.1175/BAMS-88-6-883>, 2007.
- 827 Intrieri, J. M., Shupe, M. D., Uttal, T., and McCarty, B. J.: An annual cycle of Arctic cloud characteristics observed by radar
828 and lidar at SHEBA, *Journal of Geophysical Research: Oceans*, 107, SHE 5-1-SHE 5-15,
829 <https://doi.org/10.1029/2000JC000423>, 2002.
- 830 Jimenez, C., Ansmann, A., Ohneiser, K., Griesche, H., Engelmann, R., Radenz, M., Hofer, J., Althausen, D., Knopf, D. A.,
831 Dahlke, S., Bühl, J., Baars, H., Seifert, P., and Wandinger, U.: MOSAiC studies of long-lasting mixed-phase cloud events and
832 analysis of the liquid-phase properties of Arctic clouds, *Atmospheric Chemistry and Physics*, 25, 12955–12981,
833 <https://doi.org/10.5194/acp-25-12955-2025>, 2025.



- 834 Jozef, G., Cassano, J., Dahlke, S., and de Boer, G.: Testing the efficacy of atmospheric boundary layer height detection
835 algorithms using uncrewed aircraft system data from MOSAiC, *Atmos. Meas. Tech.*, 15, 4001–4022,
836 <https://doi.org/10.5194/amt-15-4001-2022>, 2022.
- 837 Jozef, G. C., Cassano, J. J., Dahlke, S., Dice, M., Cox, C. J., and de Boer, G.: An overview of the vertical structure of the
838 atmospheric boundary layer in the central Arctic during MOSAiC, *Atmos. Chem. Phys.*, 24, 1429–1450,
839 <https://doi.org/10.5194/acp-24-1429-2024>, 2024.
- 840 Kahl, J. D.: Characteristics of the low-level temperature inversion along the Alaskan Arctic coast, *Int. J. Climatol.*, 10, 537–
841 548, <https://doi.org/10.1002/joc.3370100509>, 1990.
- 842 Karlsson, L., Baccarini, A., Duplessis, P., Baumgardner, D., Brooks, I. M., Chang, R. Y.-W., Dada, L., Dällenbach, K. R.,
843 Heikkinen, L., Krejci, R., Leitch, W. R., Leck, C., Partridge, D. G., Salter, M. E., Wernli, H., Wheeler, M. J., Schmale, J.,
844 and Zieger, P.: Physical and Chemical Properties of Cloud Droplet Residuals and Aerosol Particles During the Arctic Ocean
845 2018 Expedition, *J. Geophys. Res.-Atmos.*, 127, e2021JD036383, <https://doi.org/10.1029/2021JD036383>, 2022.
- 846 Kay, J. E., L’Ecuyer, T., Chepfer, H., Loeb, N., Morrison, A., and Cesana, G.: Recent Advances in Arctic Cloud and Climate
847 Research, *Curr Clim Change Rep*, 2, 159–169, <https://doi.org/10.1007/s40641-016-0051-9>, 2016.
- 848 Kerminen, V.-M., Chen, X., Vakkari, V., Petäjä, T., Kulmala, M., and Bianchi, F.: Atmospheric new particle formation and
849 growth: review of field observations, *Environ. Res. Lett.*, 13, 103003, <https://doi.org/10.1088/1748-9326/aadf3c>, 2018.
- 850 Koike, M., Ukita, J., Ström, J., Tunved, P., Shiobara, M., Vitale, V., Lupi, A., Baumgardner, D., Ritter, C., Hermansen, O.,
851 Yamada, K., and Pedersen, C. A.: Year-Round In Situ Measurements of Arctic Low-Level Clouds: Microphysical Properties
852 and Their Relationships With Aerosols, *Journal of Geophysical Research: Atmospheres*, 124, 1798–1822,
853 <https://doi.org/10.1029/2018JD029802>, 2019.
- 854 Kretschmar, J., Stapf, J., Klocke, D., Wendisch, M., and Quaas, J.: Employing airborne radiation and cloud microphysics
855 observations to improve cloud representation in ICON at kilometer-scale resolution in the Arctic, *Atmospheric Chemistry and
856 Physics*, 20, 13145–13165, <https://doi.org/10.5194/acp-20-13145-2020>, 2020.
- 857 Kupiszewski, P., Leck, C., Tjernström, M., Sjogren, S., Sedlar, J., Graus, M., Müller, M., Brooks, B., Swietlicki, E., Norris,
858 S., and Hansel, A.: Vertical profiling of aerosol particles and trace gases over the central Arctic Ocean during summer, *Atmos.
859 Chem. Phys.*, 13, 12405–12431, <https://doi.org/10.5194/acp-13-12405-2013>, 2013.
- 860 Lance, S., Nenes, A., Medina, J., and Smith, J. N.: Mapping the Operation of the DMT Continuous Flow CCN Counter,
861 *Aerosol Science and Technology*, 40, 242–254, <https://doi.org/10.1080/02786820500543290>, 2006.



- 862 Lannefors, H., Heintzenberg, J., and Hansson, H. C.: A comprehensive study of physical and chemical parameters of the Arctic
863 summer aerosol; results from the Swedish expedition Ymer-80, *Tellus B*, 35B, 40–54, <https://doi.org/10.1111/j.1600->
864 0889.1983.tb00006.x, 1983.
- 865 Leck, C. and Persson, C.: The central Arctic Ocean as a source of dimethyl sulfide Seasonal variability in relation to biological
866 activity, *Tellus B: Chem. Phys. Meteorol.*, 48, <https://doi.org/10.3402/tellusb.v48i2.15834>, 1996.
- 867 Lohmann, U. and Feichter, J.: Global indirect aerosol effects: a review, *Atmos. Chem. Phys.*, 5, 715–737,
868 <https://doi.org/10.5194/acp-5-715-2005>, 2005.
- 869 Lonardi, M., Akansu, E. F., Ehrlich, A., Mazzola, M., Pilz, C., Shupe, M. D., Siebert, H., and Wendisch, M.: Tethered balloon-
870 borne observations of thermal-infrared irradiance and cooling rate profiles in the Arctic atmospheric boundary layer,
871 *Atmospheric Chemistry and Physics*, 24, 1961–1978, <https://doi.org/10.5194/acp-24-1961-2024>, 2024.
- 872 Mauritsen, T., Sedlar, J., Tjernström, M., Leck, C., Martin, M., Shupe, M., Sjogren, S., Sierau, B., Persson, P. O. G., Brooks,
873 I. M., and Swietlicki, E.: An Arctic CCN-limited cloud-aerosol regime, *Atmos. Chem. Phys.*, 11, 165–173,
874 <https://doi.org/10.5194/acp-11-165-2011>, 2011.
- 875 Mayer, B. and Kylling, A.: Technical note: The libRadtran software package for radiative transfer calculations – description
876 and examples of use, *Atmos. Chem. Phys.*, 2005.
- 877 Mioche, G., Jourdan, O., Ceccaldi, M., and Delanoë, J.: Variability of mixed-phase clouds in the Arctic with a focus on the
878 Svalbard region: a study based on spaceborne active remote sensing, *Atmos. Chem. Phys.*, 15, 2445–2461,
879 <https://doi.org/10.5194/acp-15-2445-2015>, 2015.
- 880 Morales Betancourt, R. and Nenes, A.: Understanding the contributions of aerosol properties and parameterization
881 discrepancies to droplet number variability in a global climate model, *Atmospheric Chemistry and Physics*, 14, 4809–4826,
882 <https://doi.org/10.5194/acp-14-4809-2014>, 2014.
- 883 Morales, R. and Nenes, A.: Characteristic updrafts for computing distribution-averaged cloud droplet number and
884 stratocumulus cloud properties, *Journal of Geophysical Research: Atmospheres*, 115, <https://doi.org/10.1029/2009JD013233>,
885 2010.
- 886 Morrison, H., de Boer, G., Feingold, G., Harrington, J., Shupe, M. D., and Sulia, K.: Resilience of persistent Arctic mixed-
887 phase clouds, *Nature Geosci*, 5, 11–17, <https://doi.org/10.1038/ngeo1332>, 2012.
- 888 Motos, G., Freitas, G., Georgakaki, P., Wieder, J., Li, G., Aas, W., Lunder, C., Krejci, R., Pasquier, J. T., Henneberger, J.,
889 David, R. O., Ritter, C., Mohr, C., Zieger, P., and Nenes, A.: Aerosol and dynamical contributions to cloud droplet formation
890 in Arctic low-level clouds, *Atmospheric Chemistry and Physics*, 23, 13941–13956, <https://doi.org/10.5194/acp-23-13941->
891 2023, 2023.



- 892 Murto, S., Tjernström, M., Karalis, M., and Prytherch, J.: Wind, temperature, relative humidity, surface temperature and
893 radiation from expedition ARTofMELT, Arctic Ocean, 2023. Dataset version 1., [https://doi.org/10.17043/oden-artofmelt-](https://doi.org/10.17043/oden-artofmelt-2023-weather-station-1)
894 [2023-weather-station-1](https://doi.org/10.17043/oden-artofmelt-2023-weather-station-1), 2024.
- 895 Nenes, A. and Seinfeld, J. H.: Parameterization of cloud droplet formation in global climate models, *J. Geophys. Res.*, 108,
896 [2002JD002911](https://doi.org/10.1029/2002JD002911), <https://doi.org/10.1029/2002JD002911>, 2003.
- 897 Pereira Freitas, G., Kojoj, J., Mavis, C., Creamean, J., Mattsson, F., Nilsson, L., Spicker Schmidt, J., Adachi, K., Šantl-Temkiv,
898 T., Ahlberg, E., Mohr, C., Riipinen, I., and Zieger, P.: A comprehensive characterisation of natural aerosol sources in the high
899 Arctic during the onset of sea ice melt, *Faraday Discussions*, 258, 120–146, <https://doi.org/10.1039/D4FD00162A>, 2025.
- 900 Petters, M. D. and Kreidenweis, S. M.: A single parameter representation of hygroscopic growth and cloud condensation
901 nucleus activity, *Atmos. Chem. Phys.*, 11, 2007.
- 902 Pilz, C., Düsing, S., Wehner, B., Müller, T., Siebert, H., Voigtländer, J., and Lonardi, M.: CAMP: an instrumented platform
903 for balloon-borne aerosol particle studies in the lower atmosphere, *Atmos. Meas. Tech.*, 15, 6889–6905,
904 <https://doi.org/10.5194/amt-15-6889-2022>, 2022.
- 905 Pilz, C., Cassano, J. J., de Boer, G., Kirbus, B., Lonardi, M., Pöhlker, M., Shupe, M. D., Siebert, H., Wendisch, M., and
906 Wehner, B.: Tethered balloon measurements reveal enhanced aerosol occurrence aloft interacting with Arctic low-level clouds,
907 *Elem. Sci. Anth.*, 12, 00120, <https://doi.org/10.1525/elementa.2023.00120>, 2024.
- 908 Pohorsky, R., Baccarini, A., Tolu, J., Winkel, L. H. E., and Schmale, J.: Modular Multiplatform Compatible Air Measurement
909 System (MoMuCAMS): a new modular platform for boundary layer aerosol and trace gas vertical measurements in extreme
910 environments, *Atmos. Meas. Tech.*, 17, 731–754, <https://doi.org/10.5194/amt-17-731-2024>, 2024.
- 911 Prein, A. F., Mooney, P. A., and Done, J. M.: The Multi-Scale Interactions of Atmospheric Phenomenon in Mean and Extreme
912 Precipitation, *Earth's Future*, 11, e2023EF003534, <https://doi.org/10.1029/2023EF003534>, 2023.
- 913 Price, R., Baccarini, A., Schmale, J., Zieger, P., Brooks, I. M., Field, P., and Carslaw, K. S.: Late summer transition from a
914 free-tropospheric to boundary layer source of Aitken mode aerosol in the high Arctic, *Atmos. Chem. Phys.*, 23, 2927–2961,
915 <https://doi.org/10.5194/acp-23-2927-2023>, 2023.
- 916 Renard, J.-B., Dulac, F., Berthet, G., Lurton, T., Vignelles, D., Jégou, F., Tonnelier, T., Jeannot, M., Couté, B., Akiki, R.,
917 Verdier, N., Mallet, M., Gensdarmes, F., Charpentier, P., Mesmin, S., Duverger, V., Dupont, J.-C., Elias, T., Crenn, V., Sciare,
918 J., Zieger, P., Salter, M., Roberts, T., Giacomoni, J., Gobbi, M., Hamonou, E., Olafsson, H., Dagsson-Waldhauserova, P.,
919 Camy-Peyret, C., Mazel, C., Décamps, T., Piringer, M., Surcin, J., and Daugeron, D.: LOAC: a small aerosol optical
920 counter/sizer for ground-based and balloon measurements of the size distribution and nature of atmospheric particles – Part 1:
921 Principle of measurements and instrument evaluation, *Atmos. Meas. Tech.*, 9, 1721–1742, [https://doi.org/10.5194/amt-9-1721-](https://doi.org/10.5194/amt-9-1721-2016)
922 [2016](https://doi.org/10.5194/amt-9-1721-2016), 2016.



- 923 Ricchiazzi, P., Yang, S., Gautier, C., and Sowle, D.: SBDART: A Research and Teaching Software Tool for Plane-Parallel
924 Radiative Transfer in the Earth's Atmosphere, *Bull. Amer. Meteor. Soc.*, 79, 2101–2114, [https://doi.org/10.1175/1520-0477\(1998\)079%3C2101:SARATS%3E2.0.CO;2](https://doi.org/10.1175/1520-0477(1998)079%3C2101:SARATS%3E2.0.CO;2), 1998.
- 926 Roberts, G. C. and Nenes, A.: A Continuous-Flow Streamwise Thermal-Gradient CCN Chamber for Atmospheric
927 Measurements, *Aerosol Science and Technology*, 39, 206–221, <https://doi.org/10.1080/027868290913988>, 2005.
- 928 Rotstajn, L. D. and Penner, J. E.: Indirect Aerosol Forcing, Quasi Forcing, and Climate Response, *J. Climate*, 14, 2960–2975,
929 [https://doi.org/10.1175/1520-0442\(2001\)014%3C2960:IAFQFA%3E2.0.CO;2](https://doi.org/10.1175/1520-0442(2001)014%3C2960:IAFQFA%3E2.0.CO;2), 2001.
- 930 Schmale, J., Sharma, S., Decesari, S., Pernov, J., Massling, A., Hansson, H.-C., Von Salzen, K., Skov, H., Andrews, E., Quinn,
931 P. K., Upchurch, L. M., Eleftheriadis, K., Traversi, R., Gilardoni, S., Mazzola, M., Laing, J., and Hopke, P.: Pan-Arctic
932 seasonal cycles and long-term trends of aerosol properties from 10 observatories, *Atmos. Chem. Phys.*, 22, 3067–3096,
933 <https://doi.org/10.5194/acp-22-3067-2022>, 2022.
- 934 Sedlar, J.: Implications of Limited Liquid Water Path on Static Mixing within Arctic Low-Level Clouds, *Journal of Applied
935 Meteorology and Climatology*, 53, 2775–2789, <https://doi.org/10.1175/JAMC-D-14-0065.1>, 2014.
- 936 Sedlar, J., Tjernström, M., Mauritsen, T., Shupe, M. D., Brooks, I. M., Persson, P. O. G., Birch, C. E., Leck, C., Sirevaag, A.,
937 and Nicolaus, M.: A transitioning Arctic surface energy budget: the impacts of solar zenith angle, surface albedo and cloud
938 radiative forcing, *Clim Dyn*, 37, 1643–1660, <https://doi.org/10.1007/s00382-010-0937-5>, 2011.
- 939 Sedlar, J., Tjernström, M., Rinke, A., Orr, A., Cassano, J., Fettweis, X., Heinemann, G., Seefeldt, M., Solomon, A., Matthes,
940 H., Phillips, T., and Webster, S.: Confronting Arctic Troposphere, Clouds, and Surface Energy Budget Representations in
941 Regional Climate Models With Observations, *J. Geophys. Res. Atmos.*, 125, e2019JD031783,
942 <https://doi.org/10.1029/2019JD031783>, 2020.
- 943 Shettle, E. P.: Models of aerosols, clouds and precipitation for atmospheric propagation studies, *AGARD Conference
944 Proceedings*, 454, 1990.
- 945 Shupe, M. D.: Clouds at Arctic Atmospheric Observatories. Part II: Thermodynamic Phase Characteristics, *Journal of Applied
946 Meteorology and Climatology*, 50, 645–661, <https://doi.org/10.1175/2010JAMC2468.1>, 2011.
- 947 Shupe, M. D. and Intrieri, J. M.: Cloud Radiative Forcing of the Arctic Surface: The Influence of Cloud Properties, Surface
948 Albedo, and Solar Zenith Angle, *J. Clim.*, 17, 616–628, [https://doi.org/10.1175/1520-0442\(2004\)017%3C0616:CRFOTA%3E2.0.CO;2](https://doi.org/10.1175/1520-0442(2004)017%3C0616:CRFOTA%3E2.0.CO;2), 2004.
- 950 Shupe, M. D., Persson, P. O. G., Brooks, I. M., Tjernström, M., Sedlar, J., Mauritsen, T., Sjogren, S., and Leck, C.: Cloud and
951 boundary layer interactions over the Arctic sea ice in late summer, *Atmos. Chem. Phys.*, 13, 9379–9399,
952 <https://doi.org/10.5194/acp-13-9379-2013>, 2013.



- 953 Soci, C., Hersbach, H., Simmons, A., Poli, P., Bell, B., Berrisford, P., Horányi, A., Muñoz-Sabater, J., Nicolas, J., Radu, R.,
954 Schepers, D., Villaume, S., Haimberger, L., Woollen, J., Buontempo, C., and Thépaut, J.-N.: The ERA5 global reanalysis from
955 1940 to 2022, *Quarterly Journal of the Royal Meteorological Society*, 150, 4014–4048, <https://doi.org/10.1002/qj.4803>, 2024.
- 956 Solomon, A., Shupe, M. D., Persson, O., Morrison, H., Yamaguchi, T., Caldwell, P. M., and De Boer, G.: The Sensitivity of
957 Springtime Arctic Mixed-Phase Stratocumulus Clouds to Surface-Layer and Cloud-Top Inversion-Layer Moisture Sources,
958 *Journal of the Atmospheric Sciences*, 71, 574–595, <https://doi.org/10.1175/JAS-D-13-0179.1>, 2014.
- 959 Solomon, A., Shupe, M. D., Svensson, G., Barton, N. P., Batrak, Y., Bazile, E., Day, J. J., Doyle, J. D., Frank, H. P., Keeley,
960 S., Remes, T., and Tolstykh, M.: The winter central Arctic surface energy budget: A model evaluation using observations from
961 the MOSAiC campaign, *Elementa: Science of the Anthropocene*, 11, 00104, <https://doi.org/10.1525/elementa.2022.00104>,
962 2023.
- 963 Sprenger, M. and Wernli, H.: The LAGRANTO Lagrangian analysis tool – version 2.0, *Geosci. Model Dev.*, 8, 2569–2586,
964 <https://doi.org/10.5194/gmd-8-2569-2015>, 2015.
- 965 Stamnes, K., Tsay, S.-C., Wiscombe, W., and Jayaweera, K.: Numerically stable algorithm for discrete-ordinate-method
966 radiative transfer in multiple scattering and emitting layered media, *Appl. Opt.*, AO, 27, 2502–2509,
967 <https://doi.org/10.1364/AO.27.002502>, 1988.
- 968 Tjernström, M., Sedlar, J., and Shupe, M. D.: How Well Do Regional Climate Models Reproduce Radiation and Clouds in the
969 Arctic? An Evaluation of ARCMIP Simulations, *J. Appl. Meteorol. Climatol.*, 47, 2405–2422,
970 <https://doi.org/10.1175/2008JAMC1845.1>, 2008.
- 971 Vüllers, J., Achtert, P., Brooks, I. M., Tjernström, M., Prytherch, J., Burzik, A., and Neely III, R.: Meteorological and cloud
972 conditions during the Arctic Ocean 2018 expedition, *Atmospheric Chemistry and Physics*, 21, 289–314,
973 <https://doi.org/10.5194/acp-21-289-2021>, 2021.
- 974 Wehner, B., Werner, F., Ditas, F., Shaw, R. A., Kulmala, M., and Siebert, H.: Observations of new particle formation in
975 enhanced UV irradiance zones near cumulus clouds, *Atmos. Chem. Phys.*, 15, 11701–11711, <https://doi.org/10.5194/acp-15-11701-2015>, 2015.
- 977 Wendisch, M., Brückner, M., Crewell, S., Ehrlich, A., Notholt, J., Lüpkes, C., Macke, A., Burrows, J. P., Rinke, A., Quaas, J.,
978 Maturilli, M., Schemann, V., Shupe, M. D., Akansu, E. F., Barrientos-Velasco, C., Bärfuss, K., Blechschmidt, A.-M., Block,
979 K., Bougoudis, I., Bozem, H., Böckmann, C., Bracher, A., Bresson, H., Bretschneider, L., Buschmann, M., Chechin, D. G.,
980 Chylik, J., Dahlke, S., Deneke, H., Dethloff, K., Donth, T., Dorn, W., Dupuy, R., Ebell, K., Egerer, U., Engelmann, R., Eppers,
981 O., Gerdes, R., Gierens, R., Gorodetskaya, I. V., Gottschalk, M., Griesche, H., Gryanik, V. M., Handorf, D., Harm-Altstädter,
982 B., Hartmann, J., Hartmann, M., Heinold, B., Herber, A., Herrmann, H., Heygster, G., Höschel, I., Hofmann, Z., Hölemann,
983 J., Hünerbein, A., Jafariserajehlou, S., Jäkel, E., Jacobi, C., Janout, M., Jansen, F., Jourdan, O., Jurányi, Z., Kalesse-Los, H.,



984 Kanzow, T., Käthner, R., Kliesch, L. L., Klingebiel, M., Knudsen, E. M., Kovács, T., Körtker, W., Krampe, D., Kretzschmar,
985 J., Kreyling, D., Kulla, B., Kunkel, D., Lampert, A., Lauer, M., Lelli, L., Lerber, A. von, Linke, O., Löhnert, U., Lonardi, M.,
986 Losa, S. N., Losch, M., Maahn, M., Mech, M., Mei, L., Mertes, S., Metzner, E., Mewes, D., Michaelis, J., Mioche, G., Moser,
987 M., Nakoudi, K., Neggers, R., Neuber, R., Nomokonova, T., Oelker, J., Papakonstantinou-Presvelou, I., et al.: Atmospheric
988 and Surface Processes, and Feedback Mechanisms Determining Arctic Amplification: A Review of First Results and Prospects
989 of the (AC)3 Project, *BAMS*, 104, E208–E242, <https://doi.org/10.1175/BAMS-D-21-0218.1>, 2023.

990 Wu, H., Li, Z., Li, H., Luo, K., Wang, Y., Yan, P., Hu, F., Zhang, F., Sun, Y., Shang, D., Liang, C., Zhang, D., Wei, J., Wu,
991 T., Jin, X., Fan, X., Cribb, M., Fischer, M. L., Kulmala, M., and Petäjä, T.: The impact of the atmospheric turbulence-
992 development tendency on new particle formation: a common finding on three continents, *Natl. Sci. Rev.*, 8, nwaa157,
993 <https://doi.org/10.1093/nsr/nwaa157>, 2021.

994 Young McCusker, G., Vüllers, J., Achtert, P., Field, P., Day, J. J., Forbes, R., Price, R., O'Connor, E., Tjernström, M.,
995 Prytherch, J., Neely III, R., and Brooks, I. M.: Evaluating Arctic clouds modelled with the Unified Model and Integrated
996 Forecasting System, *Atmospheric Chemistry and Physics*, 23, 4819–4847, <https://doi.org/10.5194/acp-23-4819-2023>, 2023.

997